

Sep.2009 / Vol.127

MITSUBISHI ELECTRIC

ADVANCE

High Frequency and Optical Devices

- **Editorial-Chief**

Kiyoshi Takakuwa

- **Editorial Advisors**

Chisato Kobayashi
Kanae Ishida
Makoto Egashira
Koji Yasui
Hiroaki Kawachi
Masayuki Masuda
Akio Toda
Kiyoji Kawai
Tetsuji Ishikawa
Taizo Kittaka
Keiji Hatanaka
Itsuo Seki
Kazufumi Tanegashima
Kazumasa Mitsunaga

- **Vol. 127 Feature Articles Editor**

Junichiro Yamashita

- **Editorial Inquiries**

Makoto Egashira
 Corporate Total Productivity Management
 & Environmental Programs
 Fax +81-3-3218-2465

- **Product Inquiries**

Hiroaki Seki (p2-4)
 Mobile Phone Devices Marketing Sect.
 Tel: +81-3-3218-2980
 Seki.Hiroaki@cj.MitsubishiElectric.co.jp
<http://www.mitsubishichips.com/Global/>

Kazuhiko Sato (p5-16)
 High Frequency Device Marketing Sect.
 Tel: +81-3-3218-3014
 Sato.Kazuhiko@aj.MitsubishiElectric.co.jp
<http://www.mitsubishichips.com/Global/>

Jun Morita (p17-22)
 Optical Communication Devices Marketing
 Sect.
 Tel: +81-3-3218-3332
 Morita.Jun@ea.MitsubishiElectric.co.jp
<http://www.mitsubishichips.com/Global/>

Mitsubishi Electric Advance is published on
 line quarterly (in March, June, September,
 and December) by Mitsubishi Electric
 Corporation.
 Copyright © 2009 by Mitsubishi Electric
 Corporation; all rights reserved.
 Printed in Japan.

CONTENTS

Technical Reports

Overview	1
by <i>Kazuo Hayashi</i>	
A 2.4-V Low-Reference-Voltage Operation HBT-MMIC Power Amplifier Module for CDMA Applications	2
by <i>Takao Moriwaki</i> and <i>Kazuya Yamamoto</i>	
HBT High Power Amplifier Modules for WiMAX CPE Applications	5
by <i>Hitoshi Kurusu</i> and <i>Toshio Okuda</i>	
Microwave Triple Tuned Wideband VCO	8
by <i>Masaomi Tsuru</i> and <i>Ryoji Hayashi</i>	
60 W Output Power C-Band High-Efficiency Broadband GaN-HEMT	11
by <i>Yoshitsugu Yamamoto</i> and <i>Koji Yamanaka</i>	
Breakdown Voltage Enhancement in AlGaIn Channel Transistors	14
by <i>Takuma Nanjo</i> and <i>Muneyoshi Suita</i>	
High Sensitivity 2.5/10 Gbps InAlAs Avalanche Photodiodes	17
by <i>Eitaro Ishimura</i> and <i>Eiji Yagyu</i>	
43-Gbps EAM-LD Module / PD Module	20
by <i>Norio Okada</i>	

Overview



Author: *Kazuo Hayashi**

The Future of High Frequency and Optical Devices

Compound semiconductor-based high frequency and optical devices play an important role in improving the capability of information and communication systems, for which market demand is growing.

Mobile communication devices require not only a high bit rate but also multi-functionality, better performance and low power consumption. Thus, high frequency power amplifiers for transmitters are required to have low distortion, broad- or multi-band properties, multi-functionality, and low drive voltage.

High-output power amplifiers currently used for satellite communications are one of vacuum tube called a traveling wave tube amplifier (TWTA), and therefore compact, lightweight, and long service life equipment based on compound semiconductor is desired.

In the field of fixed line telecommunications, optical communication systems, which were mainly for business use, are now widely used in the home. In response to this trend, in addition to cost-effective devices, high-speed and high-sensitivity devices are being introduced for the metro and trunk line systems, which are handling increasing amounts of data communication traffic.

Mitsubishi Electric has developed and commercialized high frequency and optical devices utilizing design and manufacturing technologies acquired over the years. This issue presents our recent activities geared to these markets and technical trends.

A 2.4-V Low-Reference-Voltage Operation HBT-MMIC Power Amplifier Module for CDMA Applications

Authors: Takao Moriwaki* and Kazuya Yamamoto*

1. Introduction

This paper describes the circuit design and measurement results of the prototype HBT MMIC power amplifier module which operates with a low reference voltage of 2.4 V. The module has been developed for 900-MHz band CDMA handset applications in response to CDMA's needs for low-voltage operation.

2. Background

Recently, gallium arsenide based heterojunction bipolar transistor (GaAs-based HBT) amplifiers have been widely used for code division multiple access (CDMA) mobile handsets. To extend the battery life of such handsets, the HBT amplifier and peripheral circuits should consume minimal power. We aimed to develop a low-voltage bias circuit, which can lower the battery's end-of-discharge voltage in the handset and thus effectively prolong the battery life. However, this is not easy to achieve because the reference voltage for an emitter follower circuit generally needs to be at least twice the base-emitter voltage (V_{be} : +1.3 V).

This paper presents our new power amplifier for CDMA mobile handset applications that operates with a low reference voltage of 2.4 V. It has been made possible by: (i) dividing the RF signal power stage into two AC-coupled blocks and providing one block with a voltage and current drive bias, and the other a current

drive bias; and (ii) adding a diode linearizer to the power stage with the voltage and current drive bias to prevent deterioration of adjacent channel leakage power at low temperatures.

3. Circuit Design

Figure 1 shows a circuit block diagram of the power stage with a bias circuit for low reference voltage operation. The design target for the reference voltage was set to 2.5 V or lower so that the Si-LDO (low voltage drop out regulator) can operate even at the battery's end-of-discharge voltage of 2.7 V.

If the reference voltage is set to 2.6 V or lower, it is not sufficiently greater than twice the base-emitter voltage, and thus satisfactory operation is not expected with the emitter follower circuit used as a bias circuit for the amplifier. Therefore, a current-drive bias circuit is added to the power stage so that the desired idle current can be supplied.

In addition, in order to reduce the amount of changes in the power gain and the phase with respect to the output power and to obtain smooth and monotonic gain and phase characteristics, the power stage for amplifying RF signals is divided into two AC-coupled blocks, Tr1 and Tr2, as shown in Fig. 1. Smooth gain and phase characteristics of the power stage are important for minimizing the distortion of the amplifier,

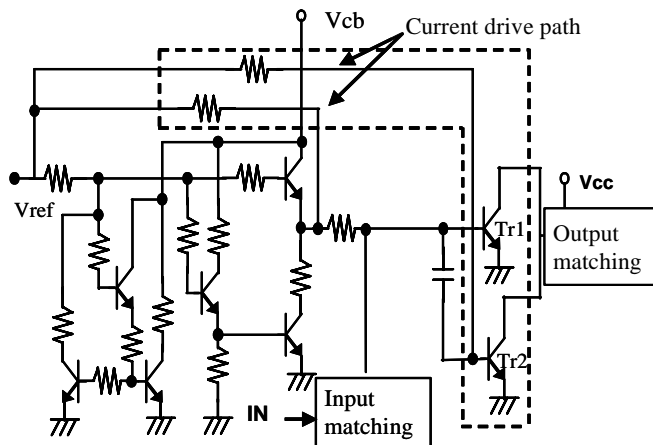


Fig. 1 Circuit configuration used for the low reference voltage operation

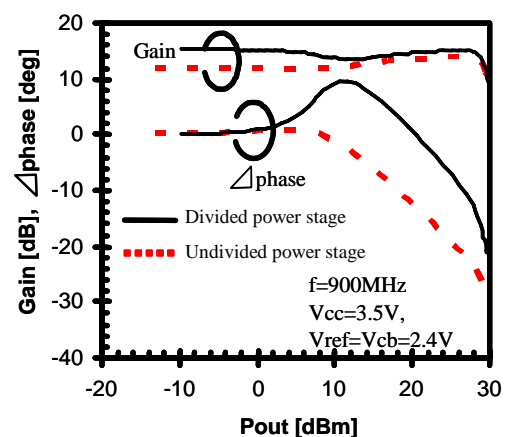


Fig. 2 Calculation results (Input-output characteristics): Comparison of divided and undivided power stages

which is a key parameter for CDMA applications. As depicted in Fig. 1, one of the divided power stage blocks, Tr1, is supplied with a base bias current through the emitter follower circuit as well as the resistor in the added current-drive supply circuit, resulting in high output operation. The other power stage block, Tr2, is supplied with a base bias current through the current-drive circuit only, to ensure the desired amount of idle current.

It was confirmed by simulation that the power stage with two kinds of bias supply circuit can achieve output characteristics having only small changes in the power gain or phase by adjusting the individual amount of supply from each current-drive base-bias circuit.

Figure 2 compares the output characteristics calculated for the circuit configurations with divided power stage (Fig. 1) and undivided power stage (Fig. 3). In these simulations, the frequency was set to 900 MHz; and as the bias conditions, the reference voltage and power supply voltage for the bias circuit were set to 2.4 V, and the collector voltage of Tr1 and Tr2 was set to 3.5 V. Figure 2 clearly shows that the divided power stage provides smooth gain and phase characteristics with respect to the output power.

However, computer simulation of the temperature dependency indicated that at low temperatures below 0°C, the circuit in Fig. 1 exhibited concave-shaped gain characteristics and convex-shaped phase characteristics similar to those of the circuit without a divided power stage. These characteristics at low temperatures were caused by the HBT's built-in base-emitter voltage that became higher than that at normal temperature, resulting in a condition similar to that when lowering the reference voltage at normal temperature.

To prevent these changes in the power gain and phase at low temperatures, a linearizer consisting of a diode and a resistor is added to the power stage as shown in Fig. 4.

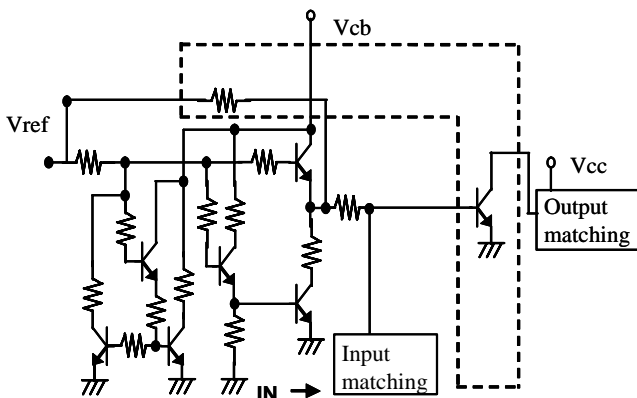


Fig. 3 Circuit configuration with an undivided power stage

Figure 5 compares the simulated output characteristics of the power stage at -10°C with and without a diode linearizer. It was confirmed that the changes in the gain and phase were effectively suppressed by adding a diode linearizer even at low temperatures.

As described above, it was confirmed by simulation that the HBT amplifier fabricated by the conventional HBT process can operate with a low reference voltage over a wide temperature range by means of the divided power stage with different bias supply methods and a diode linearizer.

4. Evaluation Results

Based on the simulation results described above, a prototype HBT monolithic microwave integrated circuit (MMIC) power amplifier module was fabricated and evaluated for the 900-MHz band J/WCDMA. A block diagram of the power amplifier module is shown in Fig. 6. The amplifier module was evaluated using 900-MHz band JCDMA (1S-95B) and WCDMA (3GPP-R99) modulation signals, and with the bias conditions of a power stage collector voltage of 3.5 V, and a power supply voltage for the bias circuit including reference voltage of 2.4 V.

The input-output characteristics with the JCDMA modulation signal are shown in Fig. 7. Results with the JCDMA modulation obtained at an output power (Pout) of 27.5 dBm were: power gain (Gp) = 26.5 dB, power added efficiency (PAE) = 40%, and adjacent channel power ratio (ACPR) = -50 dBc. These results adequately satisfy the key output characteristics required for JCDMA transmitter power amplifiers. Measurement results with the WCDMA modulation signal were Pout = 28.0 dBm, Gp = 26.7 dB, PAE = 42%, and adjacent channel leakage ratio (ACLR) = -42 dBc.

Figure 8 compares the input-output characteristics measured with and without the diode linearizer at the case temperature (Tc) = -10°C.

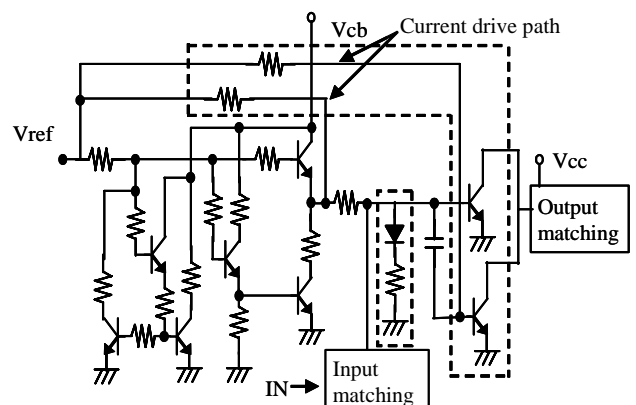


Fig. 4 Circuit configuration with a diode linearizer

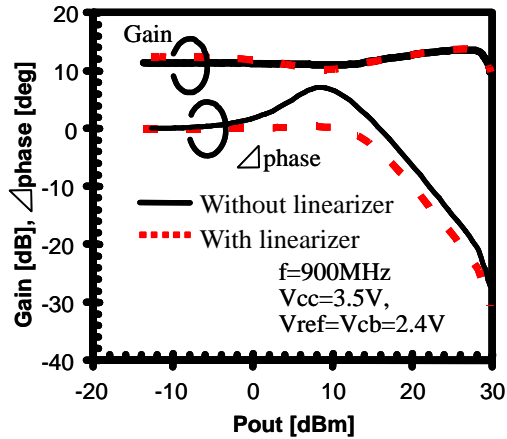


Fig. 5 Calculation results (Input-output characteristics): Comparison of characteristics with and without diode linearizer (Temperature: -10°C)

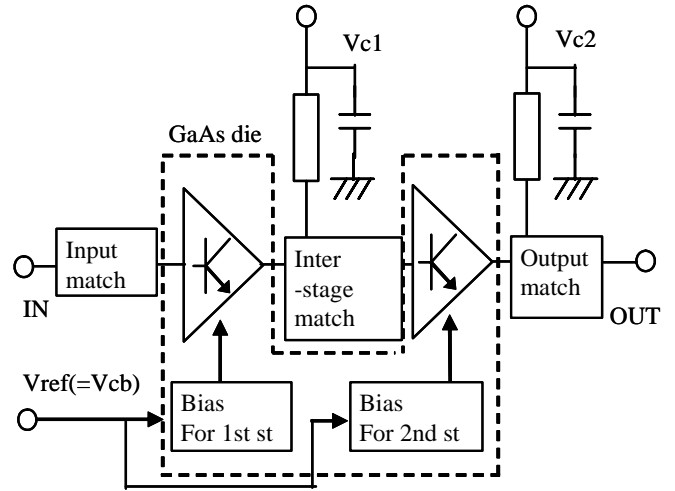


Fig. 6 Block diagram of amplifier

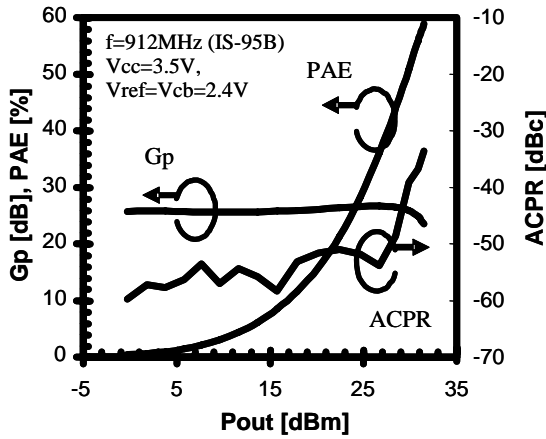


Fig. 7 Evaluation results (Input-output characteristics): JCDMA modulation ($T_c = 30^{\circ}\text{C}$)

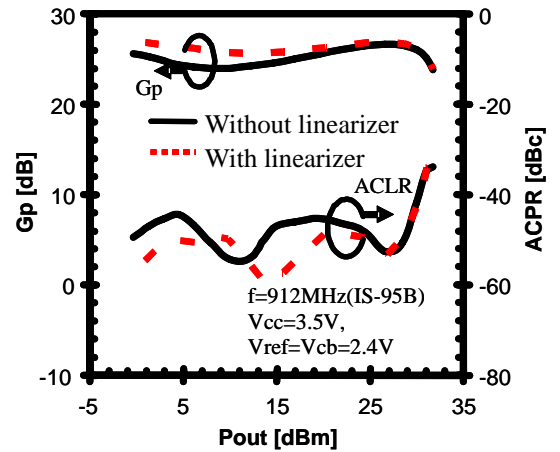


Fig. 8 Evaluation results (Input-output characteristics): Comparison of characteristics with and without diode linearizer (Temperature: -10°C)

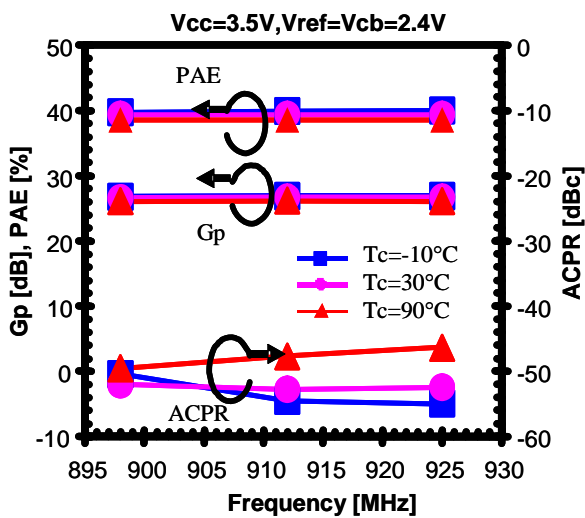


Fig. 9 Frequency characteristics with JCDMA modulation ($P_{out} = 27.5 \text{ dBm}$ [$T_c = -10^{\circ}\text{C}, 30^{\circ}\text{C}, 90^{\circ}\text{C}$])

As predicted by the previously described simulation results, if the diode linearizer is not built on the chip, the power gain significantly changes, which is associated with a significant deterioration of ACPR. In contrast, when a diode linearizer is added, flat gain characteristics are obtained with respect to the output power and ACPR is improved.

The above evaluation results clearly show, as predicted by the simulation, that our bias circuit and power stage configuration enable a lower reference voltage to be used over a wide temperature range ⁽¹⁾. We will improve the circuit design and strive to develop new amplifiers, in response to the needs for low power supply voltage.

Reference

- (1) K. Yamamoto et al., "A CDMA InGaP/GaAs-HBT MMIC Power Amplifier Module Operating with a Low Reference Voltage of 2.4 V," IEEE J. SSC, Vol. 42, No. 6, pp. 1282-1290, June 2007.

HBT High Power Amplifier Modules for WiMAX CPE Applications

Authors: Hitoshi Kurusu* and Toshio Okuda*

1. Introduction

For WiMAX power amplifier applications, we have developed three models of heterojunction bipolar transistor (HBT) power amplifier modules, MGFS36EXXXX, which all have high output power and low distortion with a 50- Ω input/output interface. These modules have an average output power of 27 dBm and a gain of 33 dB in both the 2.3- and 2.5-GHz bands with an error vector magnitude (EVM) of 2.5%, and an average output power of 25 dBm and a gain of 30 dB in the 3.5-GHz band with an EVM of 2.5%.

2. Background

Worldwide interoperability for microwave access (WiMAX) covers mid- and long-distance areas and enables high-speed communications, and thus is a promising technology for the next generation of high-speed wireless communication systems. Although different countries have allocated various frequency bands, various systems are being developed concurrently for the corresponding frequency bands. In South Korea, for example, commercial service is already available. This communication system uses an orthogonal frequency division multiplexing (OFDM) modulation signal, which has an extremely high peak output power relative to the average output power, and thus needs a power amplifier having high saturation power and low distortion characteristics. In addition, WiMAX systems for customer premises equipment (CPE) applications will be installed in PC cards and mobile handsets, and thus need to be small, low cost and operable from a single power supply.

In response to these needs, Mitsubishi Electric has developed three models of high-output-power and low-distortion HBT power amplifier modules, MGFS36EXXXX, for the 2.3-GHz, 2.5-GHz and 3.5-GHz bands, using an indium gallium phosphide/gallium arsenide (InGaP/GaAs) HBT process that is well proven for fabricating mobile phone amplifiers. On a package measuring only 4.5-mm square, the amplifier module integrates a bias circuit including amplifiers and collector power supply line, as well as functions unique to the WiMAX power amplifier such as a step attenuator and output power detector circuit using Mitsubishi's proprietary AC-coupled stack type base-collector diode switch. In addition, the 50- Ω

input/output interfaces eliminate the need for an external matching circuit and help make the overall system smaller and cheaper. The developed modules offer high output power and low distortion characteristics: the modules have an average output power of 27 dBm and a gain of 33 dB with an EVM of 2.5% in the 2.3-GHz band (MGFS36E2325) and 2.5-GHz band (MGFS36E2527), and an average output power of 25 dBm and a gain of 30 dB with an EVM of 2.5% in the 3.5-GHz band (MGFS36E3436).

3. Configuration of Power Amplifier Module

Figure 1 shows the schematic configuration of the newly developed power amplifier modules for the 2.3-, 2.5- and 3.5-GHz bands⁽¹⁾. To achieve a gain of 30 dB or greater, a three-stage amplifier is employed; and a 0/20-dB step attenuator with its control circuit and an output power detector circuit are also integrated. The bias current to each circuit is shut down by turning off the reference voltage (V_{ref}).

3.1 Step attenuator

The step attenuator consists of Mitsubishi's proprietary AC-coupled stack type base-collector diode switch (ACCS-DSW), which has a high permissible transmission power even when operating with a low bias current⁽²⁾. Figure 2 shows its circuit diagram. Under the same bias current conditions, the ACCS-DSW can improve the permissible transmission power characteristics by at least 6 dB compared to conventional diode switches. The distortion characteristics have been further improved by placing a diode linearizer at the input terminal, which compensates for the gain deviation at a high input power level.

This type of step attenuator makes it possible to insert an attenuator between the first and second stages of the amplifier, and to prevent a change in the input return loss and deterioration in the noise figure (NF) characteristics while the attenuator is being turned on and off.

The control circuit for the step attenuator is configured to allow a complementary signal to be output according to the control signal (0/3 V) input to the external control terminal (V_{cont}). A power supply switch transistor is added to the control circuit so that no current is consumed by the circuit while the V_{ref} voltage is turned off.

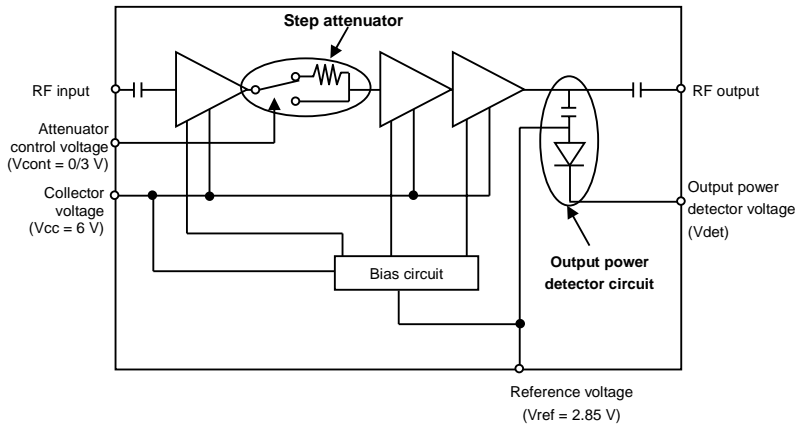


Fig. 1 Configuration of power amplifier module

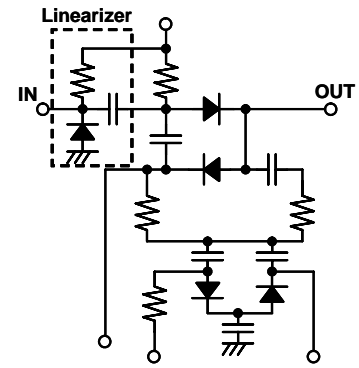


Fig. 2 Circuit diagram of step attenuator

3.2 Output power detector circuit

A diode detector circuit is used as the output power detection circuit. The circuit is designed to provide a change in the detector output voltage (V_{det}) of at least 1 V when the output power level changes from 7 to 27 dBm. This detector circuit is biased directly by the V_{ref} terminal via a resistor, and thus can also be shut down by turning off the V_{ref} voltage.

4. Basic Characteristics of Power Amplifier Module

Figure 3 shows a photograph of the WiMAX power amplifier module. A small module size of $4.5 \times 4.5 \times 1.0 \text{ mm}^3$ common to all the 2.3-, 2.5- and 3.5-GHz bands has been

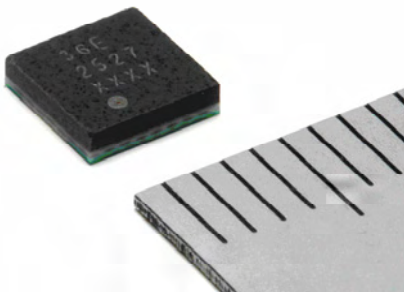
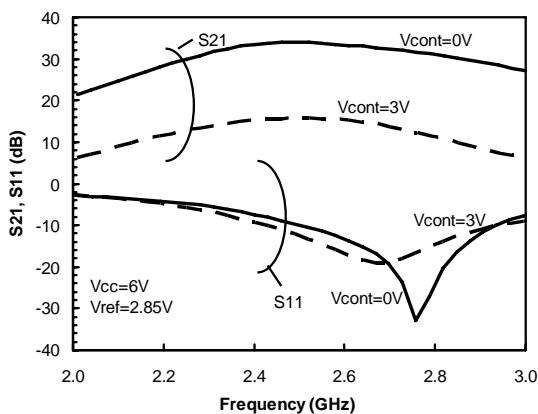


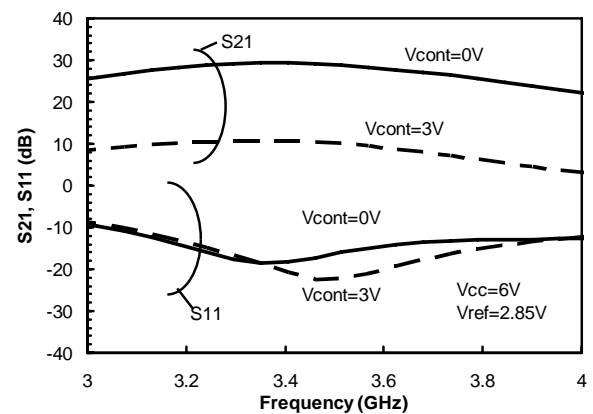
Fig. 3 Photograph of module

achieved. The InGaP/GaAs HBT process was used to fabricate the monolithic microwave integrated circuit (MMIC) power amplifier, which is mounted on the module. Figure 4 shows the measured frequency characteristics of the 2.5- and 3.5-GHz band modules with the attenuation being switched on or off and a power supply voltage of 6 V. The 2.5-GHz band power amplifier module exhibited a linear gain of at least 28 dB and an attenuation of 19 dB at frequencies between 2.5 and 2.7 GHz, and maintained an input return loss of 10 dB or greater regardless of whether the attenuation was turned on or off. The 2.3-GHz band module exhibited nearly the same characteristics. Meanwhile, the 3.5-GHz band power amplifier module also exhibited a linear gain of at least 27 dB and an attenuation of 21 dB at frequencies between 3.4 and 3.6 GHz, and showed similar input return loss characteristics as the 2.5-GHz band module, maintaining an input return loss of 10 dB or greater regardless of whether the attenuation was turned on or off.

Figure 5 shows the measured output-power dependencies of the gain, efficiency and EVM of the 2.5- and 3.5-GHz band modules with the attenuation being turned on or off and using the IEEE802.16-2004 compliant 64 QAM-OFDM modulation signal. The power



(a) 2.5-GHz band module



(b) 3.5-GHz band module

Fig. 4 Frequency characteristics when attenuation is turned on or off
Attenuation off ($V_{cont} = 0 \text{ V}$), Attenuation on ($V_{cont} = 3 \text{ V}$)

supply voltage was 6 V and the reference voltage (V_{ref}) was 2.85 V. When the attenuation was turned off, the 2.5-GHz band module exhibited a power gain of 33 dB, an EVM of 2.5%, and an efficiency of 12% with an output power of 27 dBm at frequencies between 2.5 and 2.7 GHz. The 2.3-GHz band module has nearly the same characteristics. The 3.5-GHz band module exhibited a power gain of 30 dB, an EVM of 2.5%, and an efficiency of 11% with an output power of 25 dBm at frequencies between 3.4 and 3.6 GHz. The 2.3-, 2.5- and 3.5-GHz band modules have all achieved high power gain and low distortion characteristics. When the attenuation was turned on, the output power that satisfied $EVM = 2.5\%$ was a sufficiently high value of 12 dBm or greater with all three power module models.

Figure 6 shows the measured output voltage from the detector circuit. Both the 2.5- and 3.5-GHz band modules have achieved a sufficient change in the detector output voltage (V_{det}) of 1 V or greater when the output power level is changed from 7 to 27 dBm.

The basic characteristics of these three models of power amplifier modules (MGFS36EXXX) are summarized in Table 1. These modules will be useful for developing small, low-cost handsets.

We will continue to develop products with even higher output and efficiency.

References

- (1) Miyo Miyashita et al., "Fully Integrated HBT MMIC Power Amplifier Modules for Use in 2.5/3.5-GHz-Band WiMAX Applications," IEICE Technical Report, ED 2007-220.
- (2) K. Yamamoto et al., "A 0/20 dB Step Linearized Attenuator with GaAs-HBT Compatible, AC-coupled, Stack Type Base-collector Diode Switches," IEEE International Microwave Symposium Digest, pp. 1693-1696, 2006.

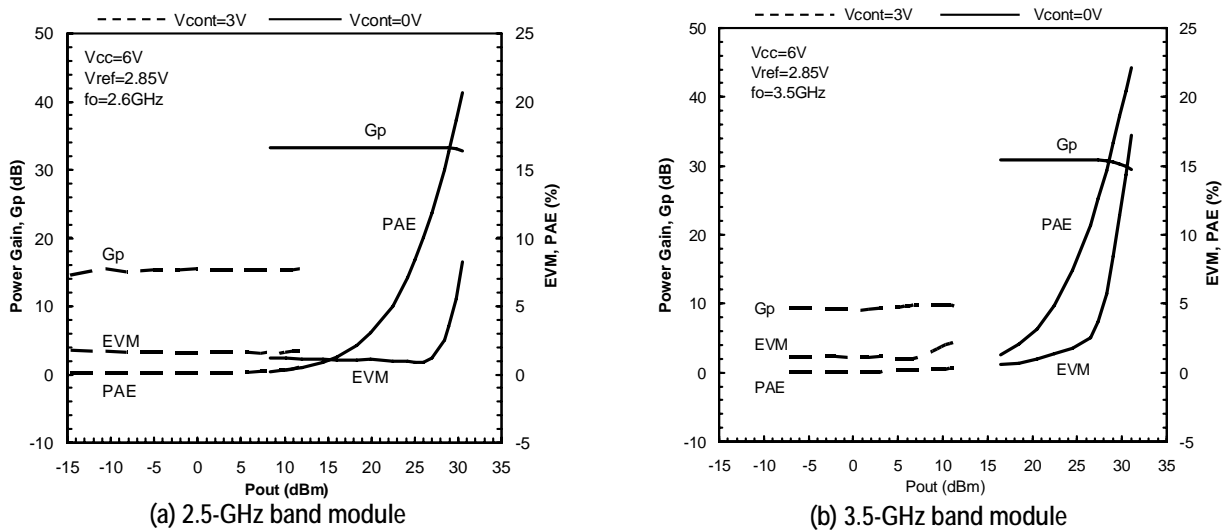


Fig. 5 Large signal characteristics when attenuation is turned on or off
Attenuation off ($V_{cont} = 0\text{ V}$), Attenuation on ($V_{cont} = 3\text{ V}$)

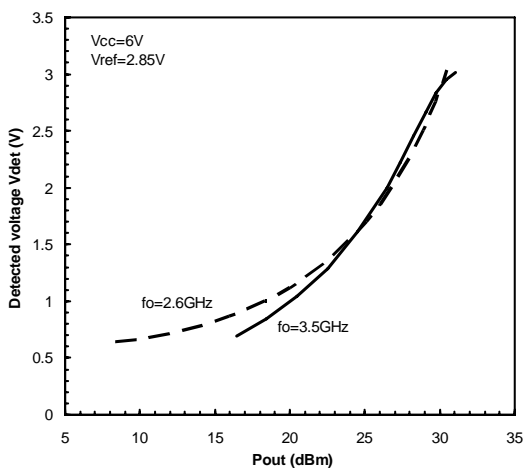


Fig. 6 Measurement result of detector output voltage

Table 1 Basic characteristics of power amplifier modules for WiMAX CPE applications

Characteristics	Measurement conditions	MGFS36E2325	MGFS36E2527	MGFS36E3436A	Unit
Operating frequency	$V_{cc} = 6\text{ V}$ $V_{ref} = 2.85\text{ V}$ IEEE802.16 signal input	2.3 – 2.5	2.5 – 2.7	3.4 – 3.6	GHz
Power gain		33	33	30	dB
Efficiency		11	12	11	%
Output power (EVM = 2.5%)		27	27	25	dBm
Input return loss		10	10	10	dB
Detector output voltage		2	2	2	V
Attenuation		16	19	21	dB
Total collector current		760	700	700	mA
Module size		4.5mm × 4.5mm × 1.0mm			

Microwave Triple Tuned Wideband VCO

Authors: Masaomi Tsuru* and Ryoji Hayashi*

1. Introduction

In this paper a triple tuned voltage controlled oscillator (VCO) is proposed for small, low-cost transceiver applications. Analytical calculations showed that the proposed VCO enables a wider oscillation bandwidth than the conventional double tuned type⁽¹⁾. A fabricated prototype exhibited a wide oscillation bandwidth of 5.6 to 16.8 GHz (relative bandwidth: 100%) and confirmed the effectiveness of the proposed configuration.

2. Configuration

Figure 1 shows the basic equivalent circuit of the triple tuned VCO. The triple tuned VCO is a series feedback oscillator consisting of one active device and three tuned circuits. In our configuration, a hetero-junction bipolar transistor (HBT) having a low 1/f noise is used as the active device. The three tuned circuits consist of a series-connected variable capacitor and inductor.

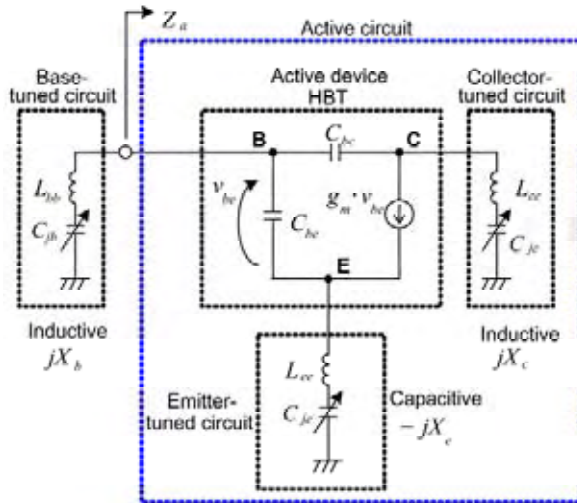


Fig. 1 Small signal equivalent circuit of the triple tuned VCO

In the basic configuration of series feedback oscillator, the tuned circuit connected either to the base or to the collector is inductive, whereas the one connected to the emitter is capacitive. A circuit consisting of an HBT and tuned circuits connected to either emitter or collector is considered to be an active circuit. Z_a is the input impedance of this active circuit when looking toward the HBT's base terminal.

3. Analysis

The following sections describe the conditions re-

quired to achieve a wide oscillation bandwidth and the relationship between the oscillation bandwidth and circuit parameters.

3.1 Conditions for wideband oscillation

If the tuned circuits are assumed to be lossless, the real and imaginary parts of Z_a are respectively expressed as the following equations:

$$\text{Re}(Z_a) = \frac{g_m \left(X_c + \frac{C_{be}}{C_{bc}} X_e \right) \cdot \left(X_c - \frac{1}{\omega C_{bc}} \right)}{\alpha^2 + \beta^2} \quad (1)$$

$$\text{Im}(Z_a) = \frac{\omega C_{be} \left(\frac{1}{\omega C_{be}} + X_e \right) \alpha - g_m X_e \beta}{\alpha^2 + \beta^2} \cdot \left(X_c - \frac{1}{\omega C_{bc}} \right) \quad (2)$$

where

$$\alpha = \omega C_{be} \left\{ \frac{1}{\omega C_{be}} + \frac{1}{\omega C_{bc}} - (X_c - X_e) \right\} \quad (3)$$

$$\beta = g_m (X_c - X_e) \quad (4)$$

The oscillation conditions are expressed as the following equations:

$$\text{Re}(Z_a) < 0 \quad (5)$$

$$\text{Im}(Z_a) + X_b = 0 \quad (6)$$

The conditions for negative resistance are derived from equations (1) and (5) and expressed as follows:

$$0 \leq X_c < \frac{1}{\omega C_{bc}} \quad (7)$$

In the case of the double tuned configuration, X_c is inductive and uncontrollable, and thus equation (7) is not satisfied at high frequencies. In the case of the triple tuned configuration, X_c can be controlled to be smaller than $1/\omega C_{bc}$. Consequently, the oscillation bandwidth of the proposed triple tuned VCO is wider than that of the double tuned VCO.

3.2 Oscillation bandwidth

Since the tuned circuit connected to the base is assumed to be lossless, $\text{Re}(Z_a)$ becomes zero in a stable oscillation state. Therefore, in a stable oscillation state, the value of g_m becomes zero and the oscillation angular frequency ω_0 is expressed by the following

equation derived from equation (6):

$$\frac{1}{X_b} = \frac{1}{\frac{1}{\omega_0 C_{be}} + X_e} + \frac{1}{\frac{1}{\omega_0 C_{bc}} - X_c} \quad (8)$$

Now, the following parameters are defined:

$$k_c \equiv \frac{C_{be}}{C_{bc}} \gg 1 \quad (9)$$

$$k_j \equiv \frac{C_{je \min}}{C_{be}} \quad (10)$$

$$n \equiv \frac{C_{je \max}}{C_{je \min}} \quad (11)$$

where $C_{j\min}$ is the minimum value of variable capacitance and $C_{j\max}$ is the maximum value of variable capacitance.

In order to control three varactor diodes using a single voltage supply, the following equations are assumed to hold:

$$C_{jc} = C_{jb} = C_{je} \quad (12)$$

In addition, since X_c and X_b are inductive and X_e is capacitive, the following equation is also assumed to hold:

$$k_l \equiv \frac{L_{cc}}{L_{ee}} = \frac{L_{bb}}{L_{ee}} > 1 \quad (13)$$

By solving equation (8), the oscillation frequency change ratio is obtained as follows:

$$\frac{\omega_{\max}}{\omega_{\min}} \approx \sqrt{n} \cdot \frac{\sqrt{2\left(1 + \frac{2}{k_l}\right) + k_j k_c \left(\frac{2}{k_c} + 1 + \frac{1}{k_l} - \sqrt{1 + \frac{2}{k_l}}\right)}}{\sqrt{2\left(1 + \frac{2}{k_l}\right) + n k_j k_c \left(\frac{2}{k_c} + 1 + \frac{1}{k_l} - \sqrt{1 + \frac{2}{k_l}}\right)}} \quad (14)$$

where the following approximation is used.

$$\chi \equiv \sqrt{\left\{2(k_l - 1) + \frac{(2k_l - k_c)C_{je}}{C_{be}}\right\}^2 + \frac{k_l(k_l + 2)k_c^2 C_{je}^2}{C_{be}^2}} \approx 2(k_l - 1) + \frac{k_c C_{je}}{C_{be}} \sqrt{k_l(k_l + 2)} \quad (15)$$

Figure 2 shows the calculation results of the oscillation bandwidth versus capacitance ratio. Equation (14) was used for the calculations. It is understood from Fig. 2 that an oscillation bandwidth of 100% is obtained when k_j is 0.05 and n is approx. 14. Figure 2 also indicates that a smaller k_j provides a wider oscillation bandwidth. Therefore, from equation (10), a transistor that has a large C_{bc} , and hence a larger emitter size, is better suited for a wideband VCO.

4. Prototype Fabrication Results

Figure 3 shows a configuration schematic of the fabricated triple tuned VCO. The active device is an InGaP/GaAs HBT with an emitter size of $120 \mu\text{m}^2$ and cut-off frequency of 31.6 GHz. The capacitance ratio of the varactor diode is approx. 13.6 with a reverse voltage between 0 and +16 V. All varactor diodes are controlled using a single voltage source.

Figure 4 shows a photograph of the fabricated triple tuned VCO. Because of high frequency operation and to prevent errors in fabricating the VCO, the HBT and varactor diodes are mounted on an alumina substrate using flip-chip technology. The size of the VCO is $8.6 \text{ mm} \times 6.8 \text{ mm}$.

Figure 5 shows the measured oscillation frequency of the fabricated VCO. Bias voltages of the HBT are $V_c = 3 \text{ V}$, $V_b = 0.3 \text{ V}$, and $V_e = -1 \text{ V}$.

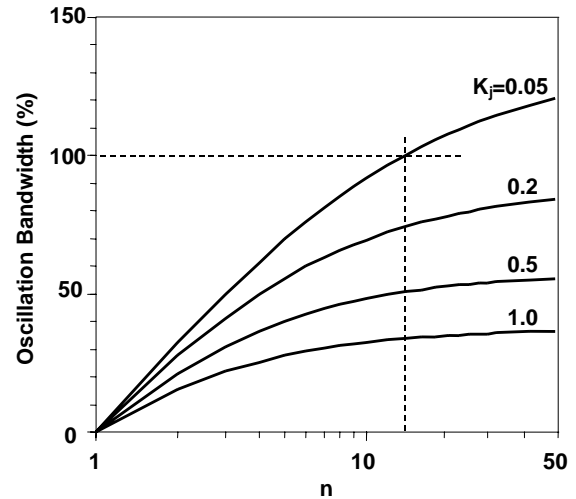


Fig. 2 Calculation results of the oscillation bandwidth versus capacitance ratio of the tuned capacitance: $k_c = 28$, $k_l = 6$

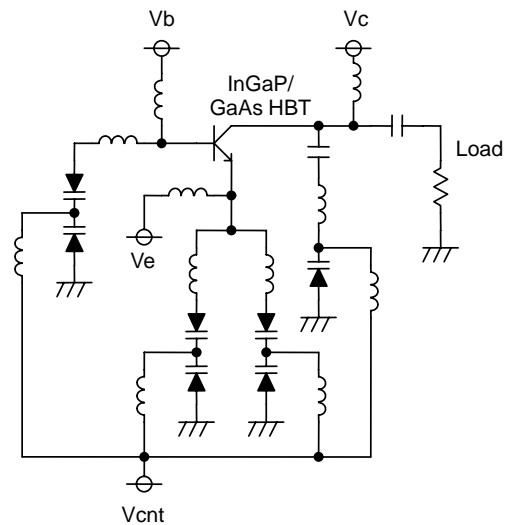


Fig. 3 Configuration of the fabricated triple tuned VCO

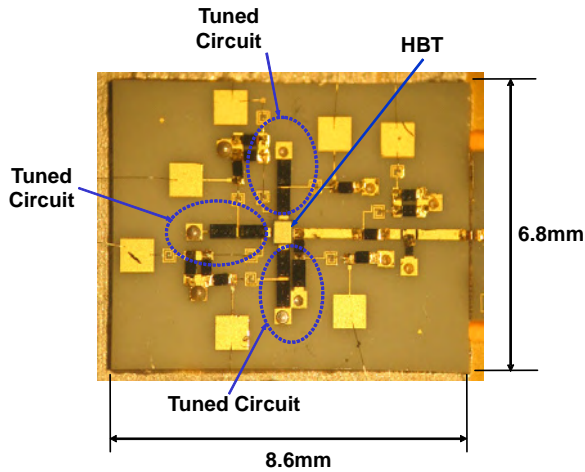


Fig. 4 Photograph of the fabricated triple tuned VCO

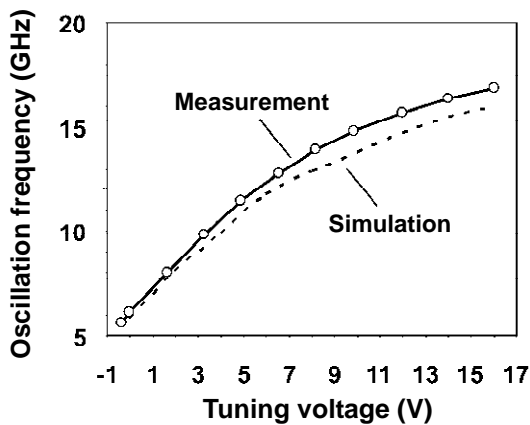


Fig. 5 Measurement results of the oscillation frequency of the fabricated VCO

Corresponding to the tuning voltage, V_{ctrl} , of -0.35 V to $+16$ V, the oscillation frequency varied from 5.6 GHz to 16.8 GHz (relative bandwidth: 100%), the phase noise was -112.0 dBc/Hz or lower at 1 MHz offset from the carrier, and the output power was 3.4 dBm \pm 2.0 dB. The current consumption was 76.1 mA or lower. The measurement results are in close agreement with the calculation result, confirming the effectiveness of this configuration.

VCOs incorporating our technology are expected to be used in a wide variety of applications.

Reference

- (1) K. Tajima, Y. Imai, Y. Kanagawa, and K. Itoh, "A 5 to 10 GHz Low Spurious Triple Tuned Type PLL Synthesizer Driven by Frequency Converted DDS Unit," IEEE MTT-S International Microwave Symposium Digest, vol. 3, pp. 1217-1220, Jun. 1997

60 W Output Power C-Band High-Efficiency Broadband GaN-HEMT

Authors: Yoshitsugu Yamamoto* and Koji Yamanaka**

The AlGaIn/GaN high electron mobility transistor (HEMT) has superior characteristics of high-voltage, high-power density, and high-frequency operation, and is expected to be used for next-generation high-power devices. To date, traveling wave tube amplifiers (TWTAs) have been widely used as high-power devices for C-band or higher frequency applications, but are now expected to be replaced by GaN-HEMT thanks to its improved performance. We have recently demonstrated superior characteristics of GaN-HEMT with an output power of over 60 W and power added efficiency of over 50% with relative bandwidth of 10%, confirming that GaN-HEMT is a promising high-power device at C-band and higher frequency.

1. Introduction

High-frequency devices are now desired to have, in addition to high power and high performance, improved characteristics for practical applications such as small size, low power consumption, high reliability and low cost. Recently, silicon laterally diffused metal-oxide semiconductors (Si-LDMOSs) are widely used as high-output-power devices for mobile phone base stations and other applications, establishing their presence in the L/S band field. Meanwhile, for C-band or higher frequency applications, gallium arsenide (GaAs) based field effect transistors (FETs) and TWTAs are widely used as high-power devices. However, the former has an upper limit of output power density because of its low breakdown voltage, making it difficult to fabricate high-power or broadband devices; and the latter has problems such as large equipment size and short life time. Therefore, new devices that solve these problems need to be developed, such as GaN-HEMT. Because of its material properties, GaN-HEMT is capable of high-voltage and high-power-density operation, and thus small, highly efficient and wide-band devices are easily achievable. Consequently, if TWTA-comparable efficiency is to be achieved in addition to the good inherent reliability of solid-state devices, GaN-HEMT would even replace TWTA.

2. Challenges for High-frequency Applications

Currently, TWTAs are widely used as C-band or higher frequency and over 100-W class high-power de-

vices, and achieve operating efficiencies exceeding 70%. To verify the advantage of GaN-HEMT for high-frequency operation, TWTA-comparable performance needs to be demonstrated. Although a C-band GaN-HEMT with an output power of over 100 W has already been reported⁽¹⁾, the device had a low efficiency and needs to be improved. In addition, when the device is used for a high-power communications amplifier, it is also important to have a wide operation bandwidth and provide a stable high performance. With these backgrounds, we have worked on improving the characteristics of GaN-HEMT devices and have developed a broadband internal matching circuit, and demonstrated its high efficiency at C-band with a relative bandwidth of about 10%.

3. Improvement of Transistor Structure

To enhance transistor performance, it is important to improve the drain efficiency and operational gain. We have already successfully prevented the current collapse phenomenon by forming a surface passivation film using catalytic chemical vapor deposition (Cat-CVD)⁽²⁾, improved the pulse I-V characteristics, and reduced the on-resistance by reducing the ohmic contact resistance by means of Si ion implantation⁽³⁾. With these efforts, the drain efficiency of the transistor has been improved, but parasitic effects become dominant at higher frequency. Consequently, to improve the performance, we have developed a transistor having via holes to reduce source inductance. Considering heat management, the newly developed transistor is fabricated on a highly heat conductive SiC substrate. However, SiC is a very hard material and difficult to process, and thus via holes can not be easily formed through thick SiC substrate. To overcome this problem, we have developed new technologies to reduce the thickness of the SiC substrate with high precision and to perform high-speed etching of via holes.

Figure 1 shows an image of a via hole (80 μm di-

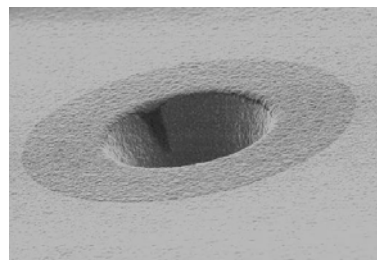


Fig. 1 SEM image of via hole

ameter) observed by a scanning electron microscope (SEM). Before we fabricated the transistor with via holes, we confirmed that good shape via holes as shown in the photograph could be stably formed without residue.

Then, we formed via holes on an actual transistor and confirmed the improvement in the gain. Figure 2 shows the device characteristics with and without via holes. The evaluated device has a gate width of 0.6 mm, and operates at a C-band frequency with a drain voltage of 50 V and a drain current of 30 mA/mm. Even without via holes, the transistor operates at high efficiency with a drain efficiency of 73%, which is calculated from the power added efficiency (PAE) and the gain at the saturated output power level. By forming via holes, the parasitic inductance is reduced, and both operational gain and maximum PAE are respectively improved by about 2 dB and 4% at the saturated output power level. These effects are likely to be even greater above C-band frequencies, and to be extremely useful for further high frequency applications in the future.

4. Development of Broadband High-Efficiency Matching Circuit

With regard to the improvement of transistor efficiency, we verified that the drain efficiency of the transistor itself was improved, and that the efficiency was boosted by improving the gain due to the reduced parasitic effect by forming via holes. However, for use as a high-power amplifier, the efficiency needs to be improved further by optimizing the internal matching circuit. In particular, if higher harmonics are generated and output from the transistor, they will reduce the efficiency. The loss in the matching circuit itself also needs to be minimized. Consequently, we have worked on improving the efficiency by effectively reflecting higher harmonics other than the fundamental wave by means of a higher harmonic reflection circuit⁽⁴⁾⁽⁵⁾. Figure 3 shows a schematic diagram of the output matching circuit that achieves high efficiency over a wide bandwidth. A second harmonic reflection circuit is directly connected to the transistor and reflects higher harmonics generated in the transistor. The reflection circuit uses parallel-connected short and

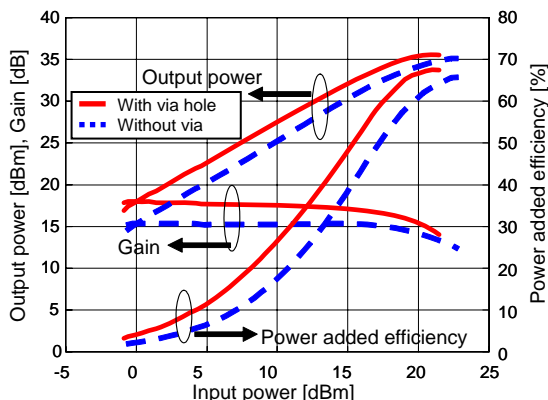


Fig. 2 Comparison of device characteristics with and without via holes

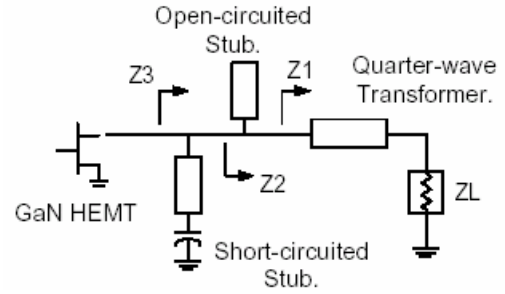


Fig. 3 Broadband high-efficiency output matching circuit

open-circuited stubs for effective reflection within the circuit. With this configuration, second harmonic waves generated in the transistor are reflected back to the transistor with very little attenuation. In addition, by appropriately setting the design parameters of the short- and open-circuited stubs, the phase condition for second harmonic reflection is satisfied over a wide bandwidth. Figure 4 shows the evaluation results of the frequency dependencies of the output power, drain efficiency, and power added efficiency of an internal matching type amplifier using the above-described transistor and matching circuit. The horizontal axis indicates the frequency ratio with respect to the center measurement frequency in C-band, F_0 . For this prototype evaluation, a transistor without via holes having a gate width of 16 mm was used, and the drain voltage was 40 V during the measurement.

These results confirm that the circuit shown in Fig. 3 effectively functions as a broadband high-efficiency output matching circuit, achieving a drain efficiency of over 53% and an output power of over 60 W across a relative bandwidth of 10% at C-band.

These results are characteristics of the transistor without via holes, so we then fabricated a device using a transistor with via holes. For this prototype, the internal matching circuit was redesigned to be optimized for the transistor with via holes. Figure 5 shows the evaluation results of the frequency dependencies of the output power and power added efficiency of a broadband high-efficiency amplifier using a transistor with via holes. The horizontal axis indicates the normalized frequency with respect to the center frequency in C-band. During

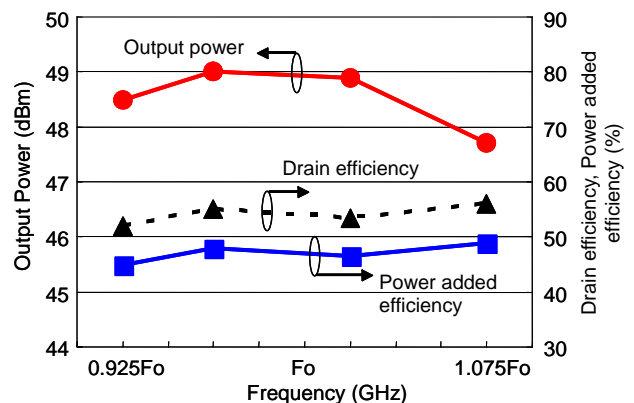


Fig. 4 Frequency characteristics of broadband high-efficiency amplifier

these measurements the drain voltage was 40 V. This chart confirms that the prototype has an output power of over 60 W and a power added efficiency of over 50% across a relative bandwidth of 10% at C-band.

Figure 6 compares these results with the reported values of C-band high-efficiency high power amplifiers (HPAs)^{(6) - (12)}. The horizontal axis shows the output power and the vertical axis the drain efficiency. Our newly developed broadband HPAs exhibit high efficiency over a wide bandwidth at C-band and have achieved the highest drain efficiency among broadband devices. These results indicate that GaN-HEMT devices offer excellent potential even at frequencies higher than C-band.

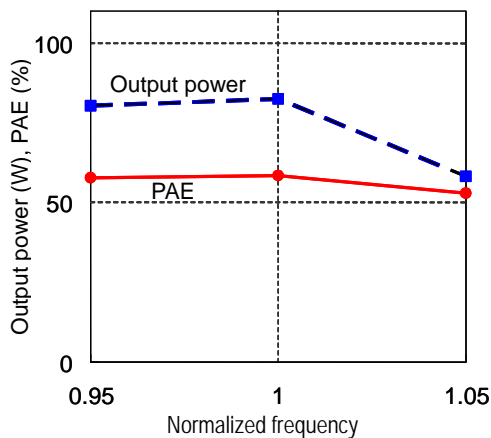


Fig. 5 Frequency characteristics of broadband high-efficiency amplifier using a transistor with via holes

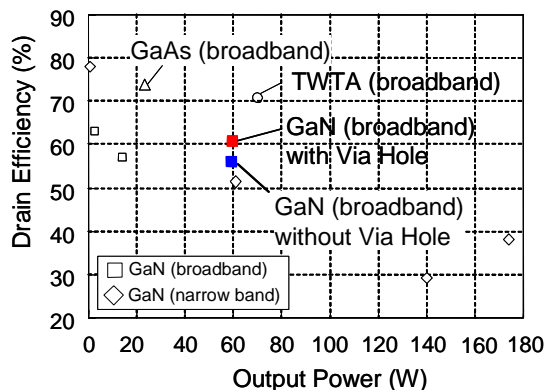


Fig. 6 Performance comparison of C-band high-efficiency amplifiers

5. Conclusion

We have developed C-band high-power broadband amplifiers using AlGaIn/GaN HEMT. We developed via hole forming technology to reduce the parasitic inductance of the transistor, and successfully demonstrated an improved operational gain. We combined this improved transistor with our newly developed broadband high-efficiency matching circuit to realize a high-frequency, broadband power amplifier device, which has the world's highest power added efficiency of over

50% with an output power of over 60 W across a relative bandwidth of 10% at C-band. These results indicate that GaN-HEMT devices are promising for operation at frequencies higher than C-band, with power and efficiency comparable with those of TWTA devices.

References

- (1) Yamanaka, K., et al.: "S and C-Band Over 100 W GaN HEMT 1 Chip High Power Amplifiers with Cell Division Configuration," 2005 European Gallium Arsenide and Other Semiconductor Application Symposium, pp. 241-244 (2005)
- (2) Kamo, Y., et al.: "A C-Band AlGaIn/GaN HEMT with Cat-CVD SiN Passivation Developed for an Over 100W Operation," Mitsubishi Technical Report, 80, No. 5, 35-38 (2006)
- (3) Oishi, T., et al.: "High Performance GaN Transistors with Ion Implantation Doping," Mitsubishi Technical Report, 79, No. 8, 39-42 (2005)
- (4) Yamanaka, K., et al.: "C-band GaN HEMT Power Amplifier with 220 W Output Power," 2007 IEEE MTT-S Int. Microwave Symp. Dig. TH1A-2 (2007)
- (5) Iyomasa, K., et al.: "GaN HEMT 60 W Output Power Amplifier with Over 50% Efficiency at C-Band 15% Relative Bandwidth Using Combined Short and Open Circuited Stubs," 2007 IEEE MTT-S Int. Microwave Symp. Dig. TH1A-3 (2007)
- (6) Ui, N., et al.: "A 100 W Class-E GaN HEMT with 75% Drain Efficiency at 2 GHz," Proc. 36th European Microwave Conf., Manchester (2006)
- (7) Colantonio, P., et al.: "A C-band High-efficiency Second-harmonic-tuned Hybrid Power Amplifier in GaN Technology," IEEE Trans. MTT-S., Vol. 54, No. 6, pp. 2713-2722 (2006)
- (8) Otsuka, H., et al.: "Over 65% Efficiency 300 MHz Bandwidth C-band Internally-matched GaAs FET Designed with a Large-signal FET Model," 2004 IEEE MTT-S Int. Microwave Symp. Dig., pp. 521-524 (2004)
- (9) Menninger, W. L., et al.: "70% Efficient Ku-Band and C-Band TWTs for Satellite Downlinks," IEEE Trans. Electron Devices, pp. 673-678 (2005)
- (10) Wu, Y.-F., et al.: "14-W GaN-based Microwave Power Amplifiers," 2000 IEEE MTT-S Int. Microwave Symp. Dig., pp. 963-965 (2000)
- (11) Chini, A., et al.: "Power and Linearity Characteristics of Field-plate Processed-gate AlGaIn-GaN HEMTs," IEEE Electron Device Letters, pp. 229-231 (2004)
- (12) Okamoto, Y., et al.: "C-band Single-chip GaN-FET Power Amplifiers with 60-W Output Power," 2005 IEEE MTT-S Int. Microwave Symp., pp. 491-494 (2005)

Breakdown Voltage Enhancement in AlGaN Channel Transistors

Authors: Takuma Nanjo* and Muneyoshi Suita*

1. Introduction

Gallium nitride (GaN) has a high electric breakdown field, saturated electron velocity and other superior characteristics. The high electron mobility transistor (HEMT) based on aluminum gallium nitride (AlGaN)/GaN, which uses GaN as a channel layer, may have a high-density two-dimensional electron gas formed at the heterojunction interface, and thus many excellent characteristics have been reported^{(1) - (5)}. Consequently, AlGaN/GaN HEMT is expected to be used as a high-power high-frequency device for next-generation information communication system such as satellite communications and mobile communication stations. The increasing amount of information communication is likely to continue growing, with data traffic accelerating such as for high-speed wireless video communications. Such applications will require even higher power devices. One effective way of improving the output power of AlGaN/GaN HEMT is to enhance the breakdown voltage of the channel layer by using a material that has a higher electric breakdown field than GaN. AlN has a band gap about twice that of GaN, hence about four times greater breakdown field. In addition, the saturated electron velocity of AlN, which affects the drain current, is nearly the same as that of GaN. Consequently, the use of Al-rich AlGaN for the channel layer is expected to enhance the breakdown voltage without reducing the drain current. In this configuration, however, the Al-rich AlGaN layer may significantly increase the ohmic contact resistance. Instead, for proper operation of HEMT that uses AlGaN as the channel layer (AlGaN channel HEMT), a new technology that reduces the contact resistance is needed.

We have already demonstrated with a conventional GaN channel HEMT that Si ion implantation doping effectively reduces the ohmic contact resistance⁽⁶⁾. This time, we have fabricated ohmic electrodes on an AlGaN channel HEMT using an Si ion implantation doping technique, and demonstrated successful transistor operation and a significantly higher breakdown voltage. This paper describes the results.

2. Experimental Method

Figure 1 shows a cross-sectional schematic view of the newly fabricated AlGaN channel HEMT. On a sapphire substrate, an AlN buffer layer was grown at high temperature, and then an unintentionally doped $\text{Al}_x\text{Ga}_{1-x}\text{N}$

channel layer and an $\text{Al}_y\text{Ga}_{1-y}\text{N}$ barrier layer were consecutively grown by metal organic chemical vapor deposition (MOCVD)⁽⁷⁾. In our experiments, two kinds of AlGaN channel structures having different Al compositions were used, namely $\text{Al}_{0.39}\text{Ga}_{0.61}\text{N} / \text{Al}_{0.16}\text{Ga}_{0.84}\text{N}$ and $\text{Al}_{0.53}\text{Ga}_{0.47}\text{N} / \text{Al}_{0.38}\text{Ga}_{0.62}\text{N}$. For comparison, a conventional epitaxial substrate with GaN channel structure ($\text{Al}_{0.18}\text{Ga}_{0.82}\text{N} / \text{GaN}$) was also fabricated.

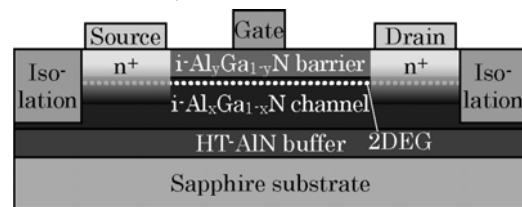


Fig. 1 A cross-sectional schematic view of the fabricated AlGaN channel HEMT

The HEMT was fabricated by forming each element in the following order: implanted contact area, source and drain electrodes, device isolation area, and gate electrode. The implanted contact area was formed by implanting ^{28}Si ions at the dose concentration of $1 \times 10^{15} \text{ cm}^{-2}$ with the implantation energy of 50 keV, followed by activation heat treatment using the rapid thermal annealing (RTA) method in a nitrogen atmosphere at 1200°C for 5 minutes. It should be noted that these ion implantation and activation heat treatment processes were performed with the semiconductor surface covered by a SiN layer. In the next stage, the source and drain electrodes were formed by depositing Ti/Al using the electron beam evaporation technique, followed by RTA treatment in a nitrogen atmosphere at 600°C for 2 minutes. Then, the device isolation area was formed by the multi-stage implantation of Zn ions⁽⁸⁾. Finally, the gate electrode was formed using Ni/Au that was deposited by the electron beam evaporation technique. Note that no surface passivation films consisting of SiN_x , for example, are formed.

3. Experimental Results

3.1 Epitaxial characteristics

Figure 2 shows the depth profile of carrier concentration in the $\text{Al}_{0.38}\text{Ga}_{0.62}\text{N}$ channel structure determined by measuring the capacitance-voltage (C-V) characteristics using Schottky diodes formed on the epitaxial substrate having the $\text{Al}_{0.38}\text{Ga}_{0.62}\text{N}$ channel layer. At a depth of about 20 nm, which nearly corresponds to the thickness of the barrier

layer, the carrier concentration abruptly increases, indicating that a two-dimensional electron gas is formed in this area. Similar results were also obtained with the other two kinds of epitaxial substrates. By integrating these carrier concentrations in the depth direction, the sheet carrier concentrations in the GaN channel, $\text{Al}_{0.16}\text{Ga}_{0.84}\text{N}$ channel and $\text{Al}_{0.38}\text{Ga}_{0.62}\text{N}$ channel structures were determined as 3.46 , 3.29 and $5.39 \times 10^{12} \text{ cm}^{-2}$, respectively. The carrier concentration at a sufficiently deep position of around $1 \mu\text{m}$ was sufficiently low at less than $1 \times 10^{14} \text{ cm}^{-3}$.

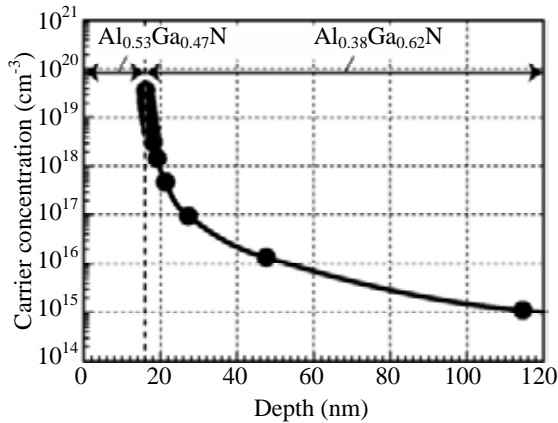


Fig. 2 Carrier concentration-depth relationship in the epitaxial substrate having $\text{Al}_{0.38}\text{Ga}_{0.62}\text{N}$ channel structure

3.2 Ohmic characteristics

Figure 3 shows the current-voltage (I-V) characteristics between the ohmic electrodes, which were formed on the two kinds of epitaxial substrates having different AlGaIn channel structures with and without Si ion implantation doping. In either epitaxial substrate, if Si ions are not implanted, the resistance is extremely high and almost no current flows. In contrast, if Si ions are implanted, the resistance is significantly reduced and the current drastically increases. Using the circular transmission line method (CTLM), the contact resistance values were determined as 1.8×10^{-5} and $5.3 \times 10^{-3} \Omega \text{ cm}^2$ on the $\text{Al}_{0.16}\text{Ga}_{0.84}\text{N}$ channel and $\text{Al}_{0.38}\text{Ga}_{0.62}\text{N}$ channel structures, respectively. As described, Si ion implantation doping may be a very effective method of forming ohmic contacts on an Al-rich $\text{Al}_y\text{Ga}_{1-y}\text{N} / \text{Al}_x\text{Ga}_{1-x}\text{N}$ heterojunction structure that has a wide band gap.

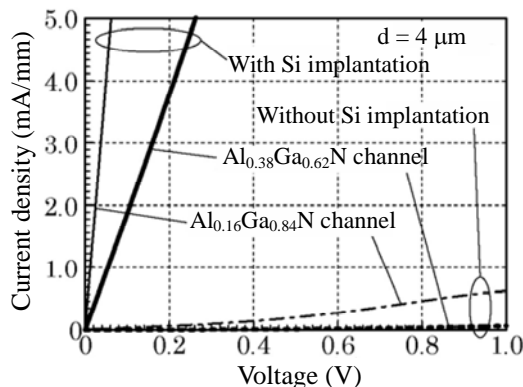


Fig. 3 I-V characteristics between the ohmic electrodes formed on various AlGaIn channel epitaxial substrates

3.3 HEMT characteristics

We used this Si ion implantation doping technique to fabricate the HEMTs and evaluated their characteristics. Figure 4 shows the drain current - drain voltage (I_d - V_d) characteristics of $\text{Al}_{0.38}\text{Ga}_{0.62}\text{N}$ channel HEMT in the on-state. The measured HEMT has a gate length (L_g) of $1 \mu\text{m}$, a gate width (W_g) of $100 \mu\text{m}$, a source-gate distance (L_{sg}) of $1 \mu\text{m}$, and gate-drain distance (L_{gd}) of $2 \mu\text{m}$. As shown in Fig. 4, this HEMT exhibited good pinch-off characteristics with the maximum drain current of 114 mA/mm . Also, the HEMTs fabricated on the other two kinds of epitaxial substrates similarly exhibited good pinch-off characteristics.

Figures 5 (a) and (b) show the I_d - V_d characteristics of three kinds of HEMTs having different L_{gd} values in the off-state, measured at a gate voltage (V_g) of -5 V . The L_g , W_g , and L_{sg} values of these samples are the same as those shown in Fig. 4. Figure 5 (a) shows the characteristics of HEMTs with an L_{gd} of $3 \mu\text{m}$, which are mainly used as high-frequency devices such as low-noise amplifiers. In comparison with the conventional type GaN channel structure, the present device structure very effectively enhances the breakdown voltage with a relatively small increase in the Al content such as 0.16 . The resulting breakdown voltage was 381 V with the $\text{Al}_{0.16}\text{Ga}_{0.84}\text{N}$ channel HEMT, and 463 V with the $\text{Al}_{0.38}\text{Ga}_{0.62}\text{N}$ channel HEMT. In contrast, Fig. 5 (b) shows the characteristics of HEMTs with an L_{gd} of $10 \mu\text{m}$, which are mainly used as high-power devices such as high-power switching devices. With this device structure, a higher Al content effectively enhances the breakdown voltage, resulting in an extremely high breakdown voltage of $1,650 \text{ V}$ with the $\text{Al}_{0.38}\text{Ga}_{0.62}\text{N}$ channel HEMT.

Figures 6 (a) and (b) respectively show the L_{gd} dependencies of the breakdown voltage and maximum drain current of the fabricated three kinds of HEMTs. As shown in Fig. 6 (a), the maximum drain current of the AlGaIn channel HEMTs is almost independent of L_{gd} , except for a small decrease when L_{gd} is over $10 \mu\text{m}$. In contrast, the breakdown voltage is significantly enhanced as the Al content is increased, and a longer L_{gd} provides

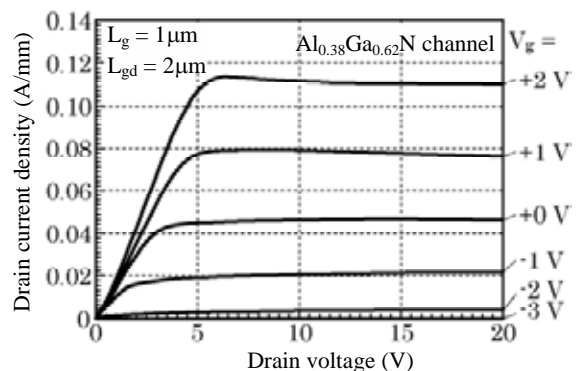
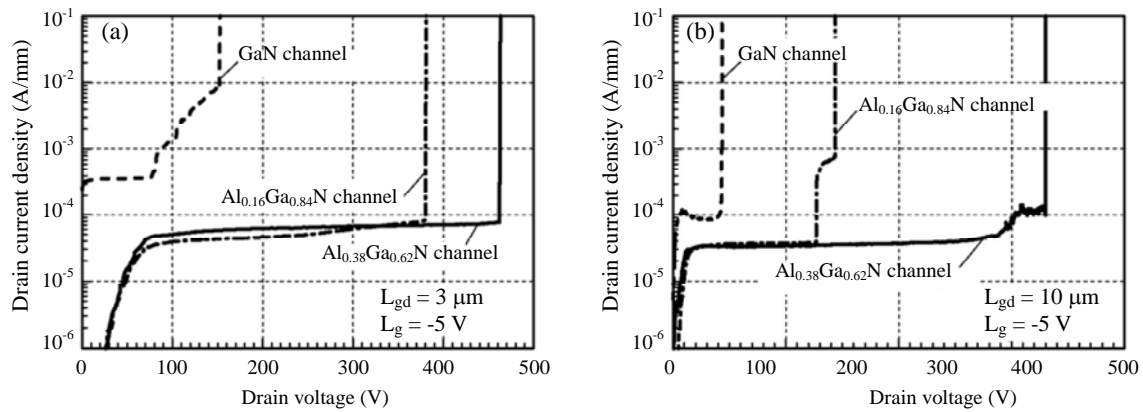
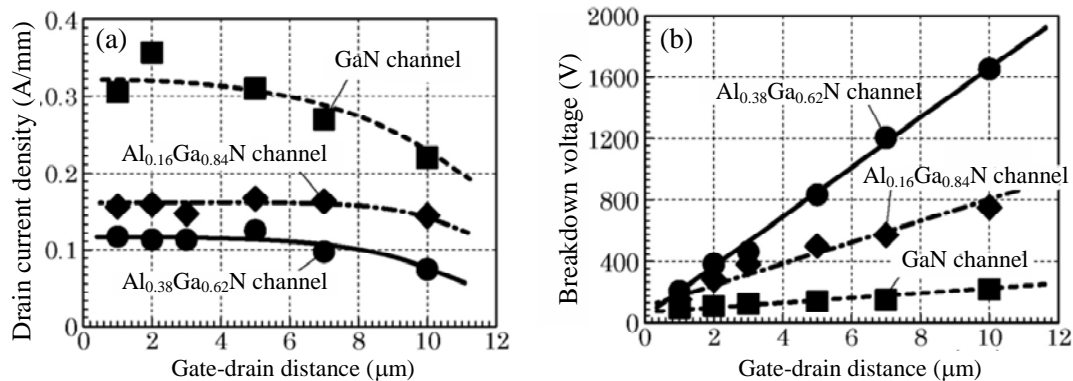


Fig. 4 I_d - V_d characteristics of the on-state $\text{Al}_{0.38}\text{Ga}_{0.62}\text{N}$ channel HEMT


 Fig. 5 I_d - V_d characteristics of the off-state HEMT

 Fig. 6 L_{gd} dependencies of maximum drain current and breakdown voltage of fabricated HEMTs

better results (Fig. 6 (b)). To the best of our knowledge, the achieved breakdown voltage is the highest among HEMTs having comparable L_{gd} lengths⁽³⁾⁻⁽⁵⁾. It is striking that these results were obtained without using any electric-field relaxation means such as a field plate structure. In other words, it may be possible to enhance the breakdown voltage even further by using such means.

4. Conclusion

To enhance the breakdown voltage of HEMT, we changed the channel layer structure from the conventional GaN to AlGa_N, and examined the characteristics of the resulting HEMTs. We achieved a reduction in the ohmic contact resistance of the source and drain electrodes by using Si ion implantation doping, and successfully demonstrated the operation of AlGa_N channel HEMT. We obtained very high breakdown voltages with the Al_{0.38}Ga_{0.62}N channel HEMTs: 463 V with a gate-drain distance of 3 μm , and 1650 V with 10 μm . To the best of our knowledge, these values are the highest achieved by HEMTs having similar structures. From these results, it is expected that the AlGa_N channel HEMT proposed in this paper will increase the output power of next-generation high-frequency devices as well as high-power devices.

5. Acknowledgements

The authors would like to thank Prof. Y. Aoyagi and Prof. M. Takeuchi of Ritsumeikan University.

References

- (1) Keller, S., et al.: Gallium Nitride Based High Power Heterojunction Field Effect Transistors: Process Development and Present Status at UCSB, IEEE Trans. Electron Devices, 48, 552-559 (2001)
- (2) Kamo, Y., et al.: "A C-Band AlGa_N/GaN HEMT with Cat-CVD SiN Passivation Developed for an Over 100W Operation," Mitsubishi Technical Report, 80, No. 5, 35-38 (2006)
- (3) Kikkawa, T.: Highly Reliable 250 W GaN High Electron Mobility Transistor Power Amplifier, Jpn. J. Appl. Phys. 44, 4896-4901 (2005)
- (4) C. S. Suh, et al.: High-Breakdown Enhancement-Mode AlGa_N/GaN HEMTs with Integrated Slant Field-Plate, in IEDM Tech. Dig. (2006)
- (5) Uemoto, Y., et al.: 8300 V Blocking Voltage Al-GaN/GaN Power HFET with Thick Poly-AlN Passivation, in IEDM Tech. Dig. (2007)
- (6) Oishi, T., et al.: "High Performance GaN Transistors with Ion Implantation Doping," Mitsubishi Technical Report, 79, No. 8, 39-42 (2005)
- (7) Takeuchi, M., et al.: Al- and N-Polar AlN Layers Grown on C-plane Sapphire Substrates by Modified Flow-modulation MOCVD, J. Cryst. Growth, 305, 360-365 (2007)
- (8) Oishi, T., et al.: Highly Resistive GaN Layers Formed by Ion Implantation of Zn Along the C Axis, J. Appl. Phys., 94, 1662-1666 (2003)

High Sensitivity 2.5/10 Gbps InAlAs Avalanche Photodiodes

Authors: Eitaro Ishimura* and Eiji Yagyu**

We have developed an InAlAs avalanche photodiode (InAlAs-APD) using a low-noise InAlAs multiplication layer that multiplies the signal. Compared to conventional InP-APD, the noise level was almost halved, and a good minimum receiver sensitivity of -29.9 dBm was achieved at 9.95 Gbps. The newly developed high-sensitivity InAlAs-APD provides sufficient characteristics for 2.5-Gbps and 10-Gbps high-sensitivity transmitter applications.

1. Structure of High-sensitivity Avalanche Photodiodes (APD)

In line with rising volumes of traffic on the Internet and other means of information communication, the speed of trunk and metro systems in Japan and overseas is being increased (from 2.5 Gbps to 10 Gbps) on the public optical-fiber communication networks. Efforts are also underway to increase the distance between repeaters, and a transmission distance of 80 km at 10 Gbps is defined in the international standard ITU-T G.691 L64.2c. Meanwhile, as fiber-to-the-home (FTTH) connections have spread, Gigabit/Ethernet Passive Optical Networks (G/E-PON) are being constructed at a rapid pace both in Japan and overseas. For the receivers used in these systems, a high-sensitivity avalanche photodiode (APD) is indispensable.

In response to the needs of these systems for a high-sensitivity light-receiving element, we have recently developed new APDs for 10-Gbps (light-receiving diameter of $20\ \mu\text{m}$) and 2.5-Gbps ($50\ \mu\text{m}$) applications. To achieve a 2 dB increase in sensitivity (i.e., higher S/N ratio) compared to previous devices, the multiplication layer that multiplies the signal was fabricated using InAlAs that generates only low excess noise during multiplication^[1-5], while a new type of planar structure was adopted to improve the reliability^[5].

Figure 1 shows the structure of the guardring-free planar type InAlAs-APD, which has been developed for 2.5/10-Gbps high-sensitivity receiver applications.

Each layer was grown by molecular beam epitaxy. First, an n-type distributed Bragg reflector layer (DBR layer) was grown on the n-type InP substrate. Then, an unintentionally doped InAlAs multiplication layer, a p-InP field control layer, an InGaAs light-absorbing layer with low carrier density, a carrier pile-up prevention layer consisting of InAlGaAs/InAlAs, and an i-InP window layer

were stacked in this order. A p-type light-receiving area was formed by the selective diffusion of zinc into the window layer. The outermost surface was protected by a SiN passivation film, which also functions as a non-reflective film. An anode electrode was formed encircling the light-receiving aperture ($20\ \mu\text{m}$ in diameter for 10 Gbps, $50\ \mu\text{m}$ for 2.5 Gbps), and then a cathode electrode was formed on the back side. This APD is a high-sensitivity type with top surface illuminated by using the light reflection from the DBR layer.

In this structure, as shown in Fig. 1, a high electric field area is confined beneath the p-type area formed by the selective diffusion and between the field control layer and the n-type layer, i.e., within the InAlAs multiplication layer, and thus no edge breakdown occurs. Although 10-nm level control needs to be performed, sufficient controllability is possible with this structure because the thicknesses of the multiplication layer and field control layer are determined by the crystal growth process.

To achieve a high speed of operation, the absorbing layer needs to be made thin, and associated low sensitivity is compensated by returning the transmitted light to the absorbing layer using a DBR layer inserted below the absorbing layer. The peak reflectivity wavelength of the DBR layer is tuned in the vicinity of 1,550 nm. Most of the 10-Gbps compatible APDs are of the back surface illuminated type, and so receive light from the substrate side and transmit light through the absorbing layer, which is reflected back by the top surface electrode. In contrast, the top surface illuminated type,

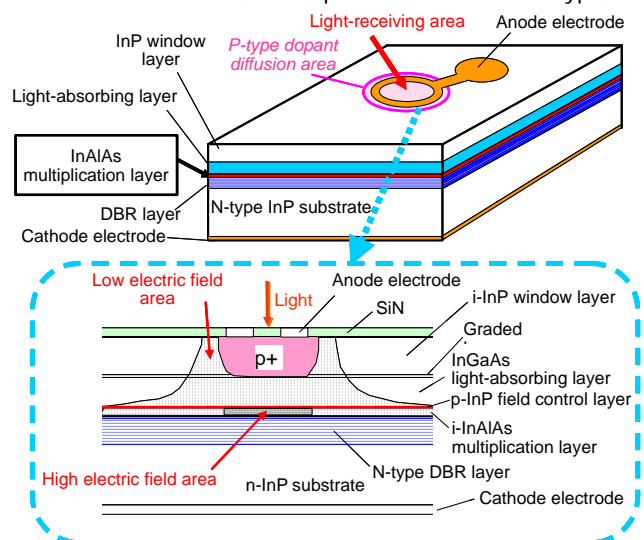


Fig. 1 Schematic diagram

which is used for the present structure, does not need any special mounting or implementation technique, and so is easy to use in combination with a preamplifier.

2. Device Characteristics

The following sections describe the device characteristics. Figure 2 shows the typical current-voltage characteristics of a 10-Gbps device with a diameter of 20 μm .

The breakdown voltage V_{br} is 28 to 32 V at 100 μA , and the dark current I_d at 90% of the breakdown voltage is as low as 10 to 20 nA. The sensitivity is as high as 0.95 A/W at the wavelength of 1.55 μm , and the chip capacitance is 0.17 pF at 90% of the breakdown voltage, which is sufficiently low for 10-Gbps applications. The -3 dB bandwidths are 10 GHz and 8.5 GHz with multiplication factors of 3 and 10, respectively, and the gain-bandwidth product is 120 GHz with multiplication factor exceeding 20. By installing the device with a preamplifier, the minimum receiver sensitivity was evaluated, providing a result of -29.9 dBm at 10 Gbps (bit error rate (BER) = 10^{-12})^[6] as shown in Fig. 3.

Characteristics of the 2.5-Gbps device with a diameter of 50 μm are now described. The breakdown voltage V_{br} is 34 to 40 V at 100 μA , and the dark current I_d at 90% of the breakdown voltage is as low as 20 to 30 nA. The sensitivity is as high as 1.0 A/W at the wavelength of 1.55 μm , and the chip capacitance is 0.27 pF at 90% of the breakdown voltage, which is sufficiently low for 2.5-Gbps applications. The -3 dB bandwidths are 5.5

GHz and 5.0 GHz with multiplication factors of 4 and 10, respectively, and the gain-bandwidth product is 70 GHz with multiplication factor exceeding 20. By installing the device with a preamplifier, the minimum receiver sensitivity was evaluated, providing a result of -36.8 dBm at 2.48 Gbps (BER = 10^{-10}) as shown in Fig. 4.

3. Realization of High Reliability

Reliability tests were performed in a nitrogen atmosphere at four temperature levels of 175°C, 200°C, 225°C and 250°C, using five samples at each temperature. Each APD was biased so that a current of 100 μA flowed corresponding to the breakdown voltage. The dark current was measured at room temperature when each device was periodically taken out of an aging test chamber. The degradation criterion was defined such that the dark current reaches 20 nA, i.e. twice the initial value. Figures 5 and 6 show the changes of dark current with time. At 225°C and 250°C, the dark current starts to increase gradually at a certain time and the devices are eventually short circuited. At 175°C and 200°C, there is no sign of degradation until 10,000 and 8,000 hours, respectively. Figure 7 shows Weibull plots for the aging tests at 225°C and 250°C.

The mean time to failure (MTTF) at 225°C and 250°C was 3,940 and 1,354 hours, respectively. The distributed parameter, m-value, was about 7 at both distributions, which indicated that the degradation mode was due to wear-out failure. Figure 8 shows an Arrhenius plot of MTTF values at each temperature. The activation

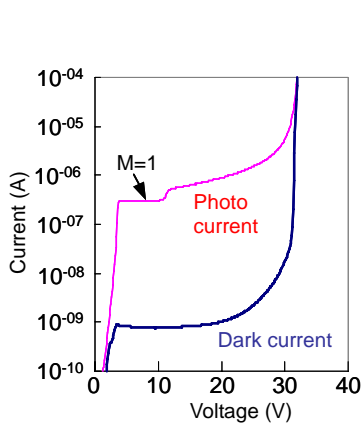


Fig. 2 Current-voltage characteristics

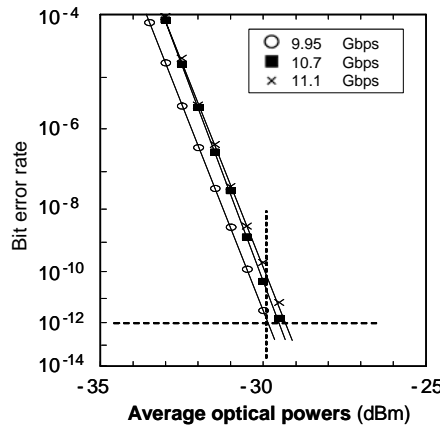


Fig. 3 10-Gbps receiving characteristics

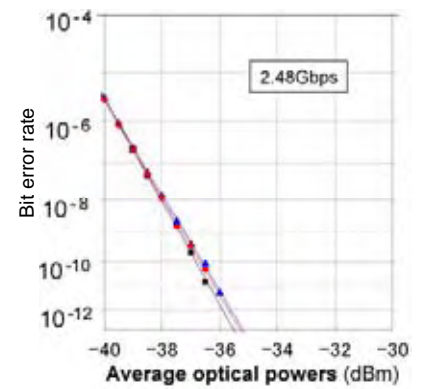


Fig. 4 2.5-Gbps receiving characteristics

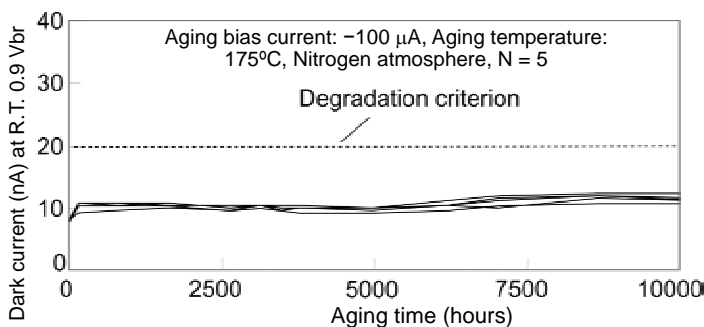


Fig. 5 Reliability test results at 175°C

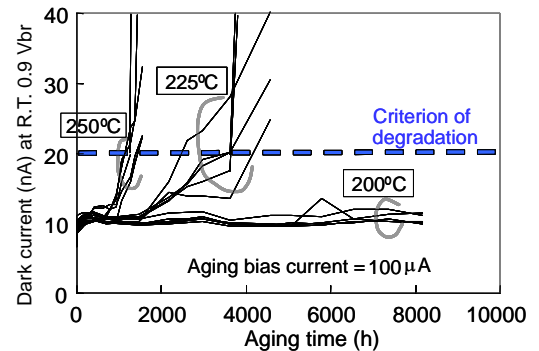


Fig. 6 Reliability test results at 200°C, 225°C and 250°C

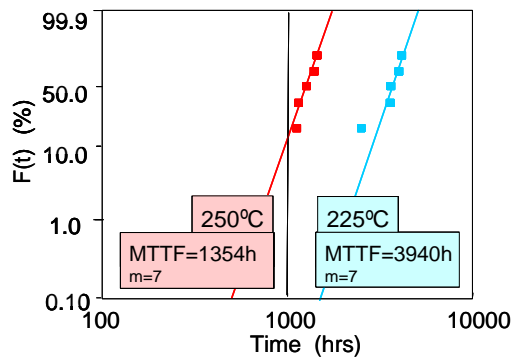


Fig. 7 Weibull plots of service life

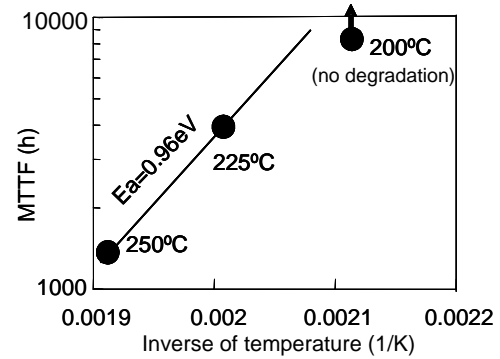


Fig. 8 Arrhenius plot of MTTF

energy determined from the MTTF values at 225°C and 250°C was 0.96 eV. Using this activation energy, the service life at 85°C was determined to be a very long time of 25 million hours. The degradation mode differs from the surface degradation reported on InP-APD^[7], where the degradation occurs in the passivation film and crystal interface with high electric field^[8, 9]. The increase in the dark current occurred in the InGaAs absorbing layer, and the degradation was observed only at a high temperature of 225°C or higher, and thus this degradation has a high activation energy and is unlikely to occur at practical operating temperatures. It is inferred that this planar structure suppresses the surface electric field, resulting in a high reliability.

4. Conclusion

As described above, we have developed InAIAs-APDs for 10-Gbps applications (light-receiving diameter of 20 μm) as well as those for 2.5-Gbps applications with a larger receiving diameter of 50 μm to facilitate module installation. To realize a high sensitivity (= high S/N ratio), we fabricated a multiplication layer that multiplies the signal using InAIAs that generates only low excess noise during multiplication. The 10-Gbps device achieved a good minimum receiver sensitivity of -29.9 dBm at 9.95 Gbps, and the 2.5-Gbps device achieved -36.8 dBm at 2.48 Gbps. In addition, we adopted a unique planar structure that is easy to fabricate and highly reliable to achieve a long-term reliability of 25 million hours (85°C), which is equivalent or better than that of InP-APD having proven reliability. The newly developed high-sensitivity 2.5-Gbps and 10-Gbps InAIAs-APDs have sufficient characteristics for high-sensitivity receiver applications. Because of their simple structure, these devices have a high production yield and thus a low cost. They are expected to be widely used for optical access networks, where low cost is a prerequisite.

References

(1) J. C. Campbell, "Recent Advances in Telecommunications Avalanche Photodiodes," *IEEE J. Lightwave Technol.*, Vol. 25, pp. 109-121, Jan. 2007.

- (2) I. Watanabe, T. Nakata, M. Tsuji, K. Makita, T. Torikai, and K. Taguchi, "High-Speed, High-Reliability Planar-Structure Superlattice Avalanche Photodiodes for 10-Gb/s Optical Receivers," *IEEE J. Lightwave Technol.*, Vol. 18, pp. 2200-2207, Dec. 2000.
- (3) S. Tanaka, S. Fujisaki, Y. Matsuoka, T. Tsuchiya, and S. Tsuji, "10 Gbit/s Avalanche Photodiodes Applicable to Non-Hermetic Receiver Modules," in *Technical Digest of Optical Fiber Communication Conf. 2003*, Vol. 1, MF55, pp. 67-68.
- (4) B. F. Levine, R. N. Sacks, J. Ko, M. Jazwiecki, J. A. Valdmanis, D. Gunther, and J. H. Meier, "A New Planar InGaAs-InAlAs Avalanche Photodiode," *IEEE Photon. Technol. Lett.*, Vol. 18, pp. 1898-1900, Sept. 2006.
- (5) E. Yagyu, E. Ishimura, M. Nakaji, T. Aoyagi, and Y. Tokuda, "Highly Productive and Reliable 10 Gb/s AllnAs Avalanche Photodiodes," in *Proc. 31st European Conf. on Optical Communications*, Vol. 3, We3. 6. 1, pp. 489-490, Sept. 2005.
- (6) E. Yagyu, E. Ishimura, M. Nakaji, H. Itamoto, Y. Mikami, T. Aoyagi, K. Yoshiara, and Y. Tokuda, "High Speed and Low Noise Guardring-Free AllnAs Avalanche Photodiode," *Proceedings 1 of the 2007 IEICE Society Conference*, C-3-42, pp. 165, Sept. 2007.
- (7) H. Sudo and M. Suzuki, "Surface Degradation Mechanism of InP/InGaAs APD's," *IEEE J. Lightwave Technol.*, Vol. 6, pp. 1496-1501, Oct. 1988.
- (8) E. Ishimura, E. Yagyu, M. Nakaji, Y. Tokuda, T. Aoyagi, and T. Ishikawa, "High Reliability of Planar Type AllnAs-APD," *2007 Spring Conference, Japan Society of Applied Physics*, 29p-SG-2, Mar. 2007.
- (9) E. Ishimura, E. Yagyu, M. Nakaji, S. Ihara, K. Yoshiara, T. Aoyagi, Y. Tokuda, and T. Ishikawa, "Degradation Mode Analysis on Highly Reliable Guardring-Free Planar InAIAs Avalanche Photodiodes," *IEEE, J. Lightwave Technol.*, Vol. 25, pp. 3686-3693, Dec. 2007.

43-Gbps EAM-LD Module / PD Module

Author: Norio Okada*

We have developed an electroabsorption modulator laser diode (EAM-LD) module with a built-in driver IC and a photodiode (PD) preamp module, both for the next-generation 40-Gbps optical communication system applications. We applied a new offset circuit design to the EAM-LD module with a built-in driver IC to reduce the load on the driver IC and also to reduce heat generation from the termination resistor, and achieved a good optical output waveform and low power consumption. In the PD preamp module, we applied an asymmetric waveguide structure to the PD, achieving a high light-receiving sensitivity and wide bandwidth, as well as a 15.3-dB dynamic range of the receiving sensitivity characteristics.

1. Module Structure

Figures 1 (a) and (b) show schematic drawings of the 43-Gbps EAM-LD module and PD module, respectively. In the 43-Gbps EAM-LD module, a built-in driver IC is integrated in one package, and GPPO™ connectors are used as the high-frequency input interface. These devices reduce the number of expensive high-frequency packages and cables, making optical transceivers smaller and cheaper. A differential electric signal input to the module is amplified by the driver IC. The operating conditions of the driver IC are adjusted to provide an optimum optical output waveform. Since the characteristics of the EAM and LD are sensitive to the temperature, a thermo-electric cooler (TEC) is used to maintain a constant temperature. The PD module has a built-in trans-impedance amplifier (TIA) to convert and amplify an optical signal to a voltage signal. The converted high-frequency signal is then AC coupled in the module and connected to the GPPO™ connectors for output. Figure 2 shows photos of the packages. The package size of the EAM-LD module is 18 mm (length) × 22 mm (width) × 8.5 mm (height) excluding the fiber and pins, and the PD module is 15 mm (length) × 22 mm (width) ×

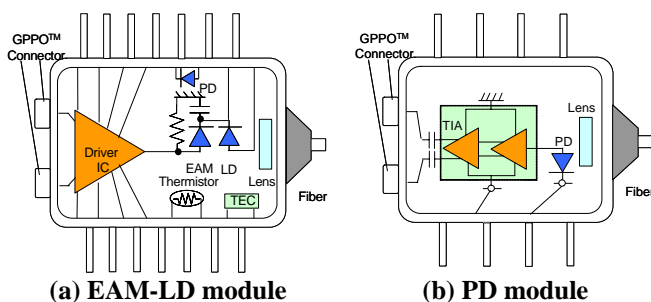


Fig. 1 Schematic drawing of modules

8.5 mm (height), both compliant with the 40 Gbit/s Miniature Device Multi Source Agreement (XLMD-MSA), which is the standard for 40-Gbps optical modules.

2. EAM-LD Module Built-in Driver IC

2.1 Design

As the operating speed of a transistor increases, collector-emitter breakdown voltage generally decreases. The driver IC for the modulator needs to be carefully designed in terms of the breakdown voltage in particular, because the IC needs to operate at high speed with a high output voltage swing.

Figure 3 shows schematic drawings of (a) the present drive circuit, (b) the DC coupled drive circuit, and (c) the bias-T drive circuit. In the conventional DC-coupled drive circuit, the EAM, termination resistor, and driver IC are DC coupled, and the voltage swing, cross point, and offset voltage (a high level voltage applied to the EAM) are adjusted by the driver IC⁽¹⁾. Considering that the EAM needs a voltage swing of 2.5 V_{pp} , and the offset voltage of the EAM is lowered to -1 V for optimizing the transmission characteristics, the collector-emitter breakdown voltage of the transistor needs to be at least 3.5 V. In the present drive circuit, an adjustable offset voltage is directly applied to the cathode of the EAM. Since no offset DC voltage is required at the anode electrode, the breakdown voltage required for the transistor can be reduced to 2.5 V. In addition, heat generation from the termination resistor is suppressed, and the power consumption of the TEC can also be reduced. Compared to the bias-T circuit, although the same collector-emitter breakdown voltage of over 2.5 V is required, the present drive circuit reduces high-frequency losses because it does not need any capacitor or coil for AC coupling to the signal line.

The operating temperature of the EAM is set to 40°C. At a high temperature, this setting reduces the difference between ambient temperature and the EAM setting temperature, thus reducing the power con-

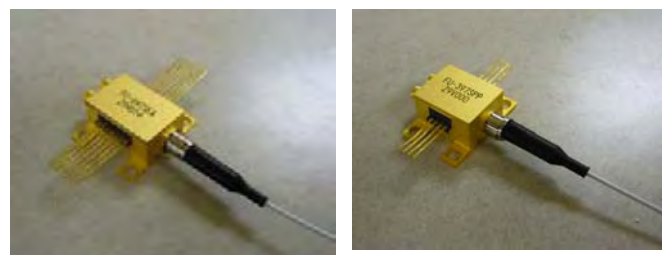


Fig. 2 Photo of modules

sumption of the TEC.

2.2 Results

The module was evaluated by connecting it to a 16:1 multiplexer (MUX). Figure 4 shows 43-Gbps optical output waveforms with the PN31 pattern when the package temperature was varied from -5°C to 80°C . The LD current was 70 mA, and the setting temperature of the TEC was 40°C . We achieved an extinction ratio of 13.8 dB to 14.1 dB (specification: 8.2 dB or greater), and a mask margin of 13% to 16% (specification: 0% or greater) using the ITU-T standard mask. Good transmission characteristics have also been achieved. As shown in Fig. 5, the evaluation results indicate the power penalty after 40 ps/nm dispersion to be 1.2 dB or lower at the full temperature range (specification: 2.0 dB or lower). Figure 6 shows the TEC power consumption. By setting the operating temperature of the EAM to 40°C and suppressing the heat generation from the termination resistor, the TEC power consumption has been suppressed to 0.70 W at a case temperature of 80°C .

3. PD Preamp Module

3.1 Design

Figure 7 shows the structure of the PD. The PD has an edge illuminated type waveguide structure to achieve wideband frequency response and high sensitivity characteristics, with the anode and cathode electrodes arranged on the same plane. Generally, in an optical waveguide, the difference in refractive index between the InP clad layer and InGaAsP optical confinement layer varies, and thus the amount of confinement varies with the wavelength. Therefore, we applied our proprietary asymmetric waveguide structure, resulting in high sensitivity at both the $1.55\ \mu\text{m}$ and $1.31\ \mu\text{m}$ wave bands.

Figure 8 shows the frequency response characteristics of the PD. A 3-dB bandwidth of over 50 GHz has been achieved at either wavelength. The light-receiving sensitivity was 0.82 A/W and 0.91 A/W at $1.31\ \mu\text{m}$ and $1.55\ \mu\text{m}$, respectively. High sensitivity and wide bandwidth have been achieved at both wavelengths^(2,3).

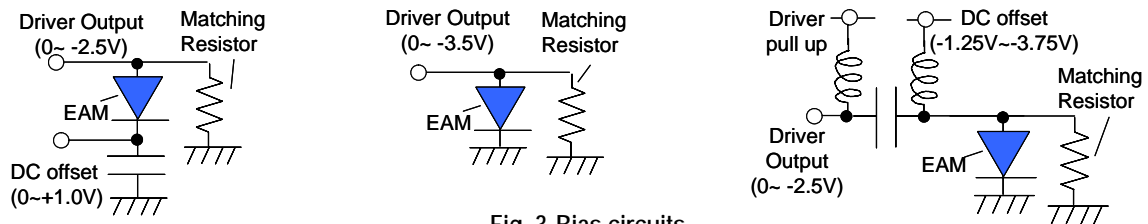


Fig. 3 Bias circuits

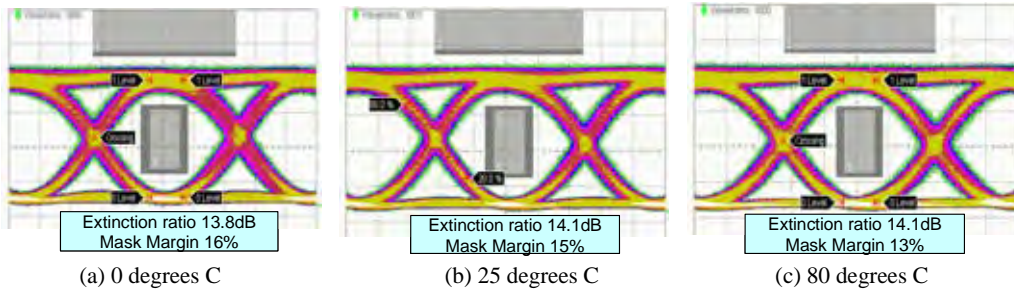


Fig. 4 43 Gbps optical output waveforms

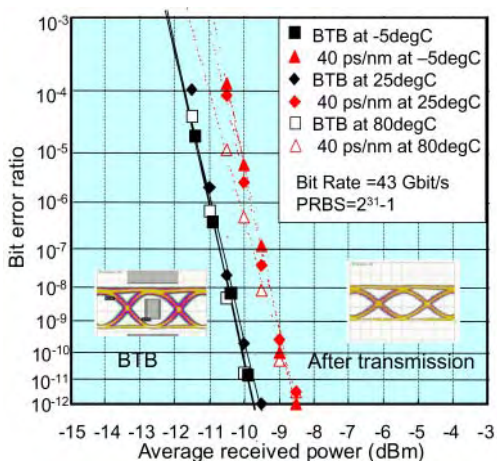


Fig. 5 Measured 43Gbps BER versus received optical power

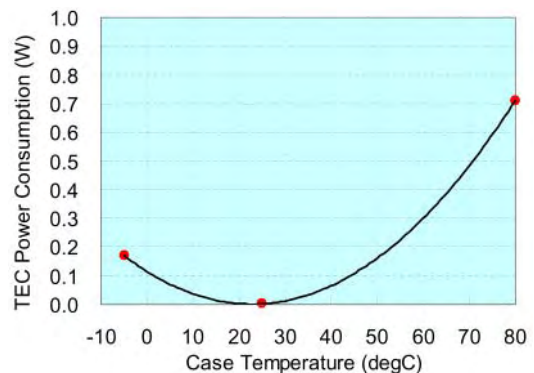


Fig. 6 TEC power consumption

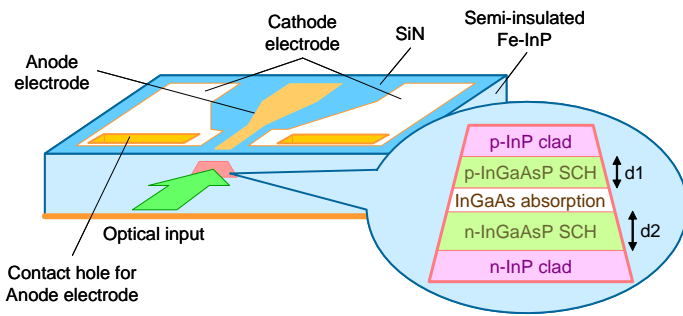


Fig. 7 Schematic drawing of PD chip

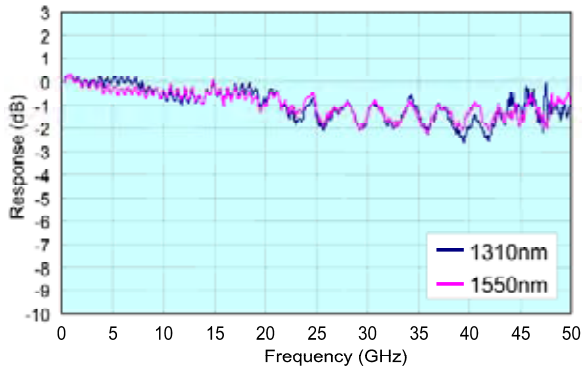


Fig. 8 Frequency response of PD chip

3.2 Results

All evaluations were performed using a light source with a wavelength of 1.55 μm . Figure 9 shows the frequency response characteristics of the PD preamp module. A good frequency response without any large ripples was achieved with a 3-dB bandwidth of 30 GHz. Figure 10 shows 43-Gbps electrical output waveforms at input levels of (a) -10 dBm and (b) +3 dBm. During either small signal or large signal operation, clear eye opening with a low jitter waveform was achieved. The small signal differential gain was 62 dB Ω . Figure 11 shows the bit error ratio with the PN31 pattern. The bit error ratio was measured with the module connected to a 1:16 demultiplexer (Demux). The error-free range, i.e. the range where the bit error ratio is 1×10^{-12} or lower,

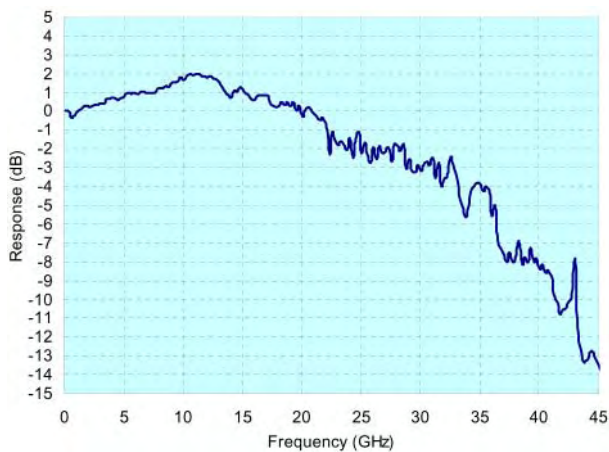


Fig. 9 Frequency response of PD preamp module

was -12.7 to -11.7 dBm for the minimum sensitivity and +3.6 to +3.7 dBm for the maximum sensitivity, both corresponding to a temperature range of -5°C to +80°C, resulting in a dynamic range of 15.3 dB. The International Telecommunications Union - Telecommunication (ITU-T) G.693 specification is -6 dBm to +3 dBm, and thus our device complies with the standards with sufficient margin. The power consumption was 0.19 W.

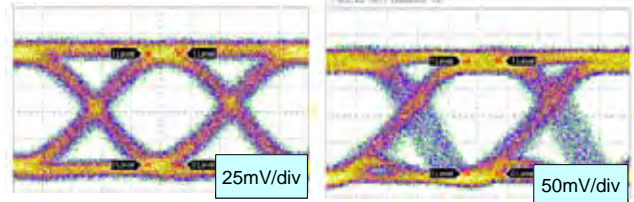


Fig. 10 43Gbps electrical output waveforms

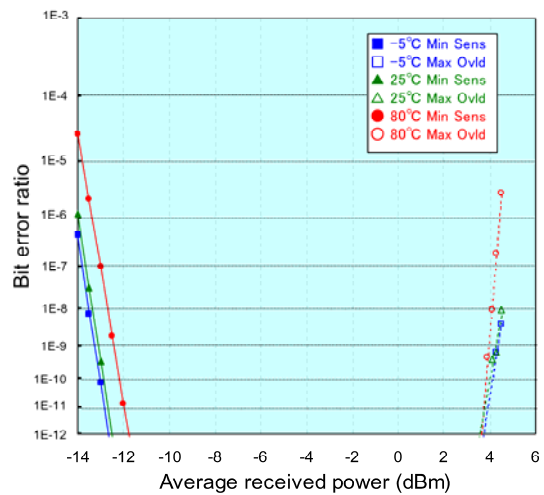


Fig. 11 BER

4. Conclusions

We have developed a 43-Gbps EAM-LD module and a PD module. Both modules exhibited good optical, high frequency and bit error ratio characteristics, in addition to much smaller size, lower power consumption, and lower cost. The newly developed products are expected to become established as core elements of next-generation optical communication technologies, and rapidly introduced for commercial applications.

References

- (1) N. Okada, et al., "0.5 Vpp-drive Small-chirp 40 Gbit/s Electroabsorption Modulator Module with Hybrid-integrated Driver IC," OFC2003, paper FO6 (2003).
- (2) S. Zaizen, et al., "40 Gbit/s PD Preamp Module for 1.3/1.55 μm Wavelength," 2003 IEICE Electronics Society Conference, C-3-138 (2003).
- (3) M. Nakaji, et al., "Asymmetric Waveguide Photodiode Over 50 GHz with High Sensitivity for Both 1.3 μm and 1.55 μm Wavelength," ECOC2003, paper Th3.4.2 (2003).

